



Partnership for Air Transportation
Noise and Emissions Reduction
An FAA/NASA/Transport Canada-
sponsored Center of Excellence



Climate Impacts of Aviation

PARTNER Project 12 final report on subtask:
Large Eddy Simulations of Contrails

prepared by
Sanjiva K. Lele, Richard C. Miake-Lye

September 2008

REPORT NO. PARTNER-COE-2008-007

Climate Impacts of Aviation

Final Report of subtask: Large Eddy Simulations of Contrails

Sanjiva K. Lele, Richard C. Miake-Lye

PARTNER-COE-2008-006

September 2008

This work was funded by the U.S. Federal Aviation Administration Office of Environment and Energy, under Grant 03-C-NE-SU. The Emissions Atmospheric Impact Project was managed by Dr. Mohan Gupta.

Any opinions, findings, and conclusions or recommendations expressed in this material are those of the author(s) and do not necessarily reflect the views of the FAA, NASA or Transport Canada.

The Partnership for AiR Transportation Noise and Emissions Reduction — PARTNER — is a cooperative aviation research organization, and an FAA/NASA/Transport Canada-sponsored Center of Excellence. PARTNER fosters breakthrough technological, operational, policy, and workforce advances for the betterment of mobility, economy, national security, and the environment. The organization's operational headquarters is at the Massachusetts Institute of Technology.

The Partnership for AiR Transportation Noise and Emissions Reduction
Massachusetts Institute of Technology, 77 Massachusetts Avenue, 37-395
Cambridge, MA 02139 USA
<http://www.partner.aero>

PARTNER PROJECT 12
CLIMATE IMPACTS OF AVIATION
FINAL REPORT ON SUBTASK: LARGE EDDY SIMULATIONS OF CONTRAILS

Project Lead Investigator

Sanjiva K. Lele
Professor of Aeronautics and Astronautics and of Mechanical Engineering
Stanford University
Mail Code 4035
Durand Building, Room 359
440 Escondido Mall
Stanford, CA 94305-4035
Tel: 650-723-7721
Fax: 650-725-3377
wmail: lele@stanford.edu

University Participants

Stanford University

- P.I.: Sanjiva K. Lele
- FAA Award Number: 03-C-NE-SU, Amendment No. TBD
- Period of Performance: June 1, 2005 to December 30, 2007
- Task: Large Eddy Simulations of Early Contrail Evolution

Aerodyne Inc.

- P.I.: Richard C. Miake-Lye
- Subcontract from Stanford University, Amendment No. TBD
- Period of Performance: June 1, 2005 – December 30, 2007
- Task: Sub-contract under the Stanford grant

This report is organized in two parts. Part I of this technical report is based on high-fidelity simulations of contrails using large-eddy simulations, work conducted at Stanford University. Part II is the detailed report on the work done at Aerodyne on detailed microphysical modeling of contrail evolution conducted with a simplified model of the flow. Technical interactions between these two efforts and with Boeing partners throughout the duration of the project helped significantly in the progress achieved.

Project Overview

The direct impact of aviation on climate via the emission of green house gases is small relative to other anthropogenic sources. [See IPCC Report (1999).] However, the potential impact of aviation on climate is unique because aviation associated sources occur at significant altitude where other anthropogenic sources are absent. Climatic impact of aviation on stratospheric ozone for a supersonic airplane fleet and the impact on radiative forcing via persistent contrails and contrail-induced cirrus clouds can be significant. There are large uncertainties in relating aviation emissions to changes in radiative forcing or surface temperature, especially for contrail-associated pathways. This research project seeks to find robust relationships between aircraft parameters (i.e., controllable inputs) and the properties of contrails generated by the aircraft under a variety of atmospheric conditions using high-fidelity numerical simulations. This project aims to develop the large-scale computational capability for the above task and assess them by comparing with other similar existing models.

Investigation Team:

Stanford University: Prof. Sanjiva K. Lele: PI

Stanford University student: Anup A Shirgaonkar (graduated Dec 2006), Ankit Bhagatwala (from July 2006, project funding ended in March 2007)

Aerodyne: Dr. Richard C. Miake-Lye: co-PI, Dr. Hsi-Wu Wong

Boeing: Dr. Steven L. Baughcum, Dr. Mikhail Danilin, Timothy Rahmes

(Boeing provided in-kind cost sharing for this PARTNER project.)

Part I: Large Eddy Simulations of Contrail Evolution

Anup A. Shirgaonkar, Sanjiva K. Lele, and Ankit Bhagatwala

Stanford University

Motivation

As described in the project overview above, the uncertainties in contrail models affect the prediction of aviation-related radiative forcing in Global Circulation Models (GCM). One of the principal sources of this uncertainty is the scale separation between the GCM grid resolution and the aircraft plume-scale processes. The contrail processes, essentially being sub-grid in a GCM setting, have to be parameterized using suitable contrail models. Large uncertainties have been attributed to these models, which motivate the current study. The objective of this work is to leverage high-resolution simulations of contrail-scale processes to find relationships between contrail properties and aircraft parameters and atmospheric conditions. Simulation data from long-term evolution of contrails can help improve and refine GCM level contrail models.

Background

Aviation's global impact on the environment is mainly related to the direct and indirect effects of aircraft emissions in the atmosphere. Contrails are one of the prime indirect effects of aircraft emissions. They occupy a unique position in this area because of their location which is in the upper troposphere/lower stratosphere region where other anthropogenic sources of emissions are absent.

Global impact of contrails: Research needs

The Intergovernmental Panel on Climate Change (IPCC) published a comprehensive status report on the global environmental impacts of aviation in 1999 (IPCC, 1999). This report constitutes a landmark effort which summarizes the status of understanding at that time, and makes many recommendations to scientists and policymakers about the needs for further research. Within PARTNER, the status of the scientific knowledge about contrails and recommendations for policymakers were made (Miake-Lye, Report No. PARTNER-COE-2005-003; Wuebbles, et al., Report No. PARTNER-COE-2006-04). All of the above findings emphasize the need for further research on particulate emissions and their atmospheric effect, including the effect of persistent contrails.

The contrail-induced RF is a significant fraction of the total aviation-induced RF, and the uncertainties in its estimation are high (IPCC, 1999; Sausen et al., 2005). These uncertainties can arise in part due to the lack of understanding of the behavior of particulate emissions in the atmosphere, and the lack of data to reliably predict their ability to act as condensation nuclei. The uncertainties in the amount and properties of particle emissions from an aircraft engine directly contribute to the inaccuracies of contrail models. Other major factors contributing to the uncertainties in contrail prediction are the uncertainty in atmospheric data (water vapor

content, ambient temperature, wind shear and turbulence), and the small-scale local thermodynamic interactions between ice nuclei and ambient fluid, which is difficult to predict.

Contrail modeling at regional and global scales

Estimates of RF resulting from contrails and aviation-induced cirrus involve uncertainties to such extents that improvements are necessary to reduce them (Lee et al, 2000). A detailed review of the status of knowledge about contrail formation, their properties and climatic effects is given by (Schumann, 2005). The incorporation of the available knowledge about contrails into global calculations is restricted to some extent by the difficulties in reliably capturing the contrail physics using simple lower-order models. In a global climate model (GCM) or a rapid update cycle (RUC) model (the latter is more relevant to the aviation industry due to its high frequency prediction capability), contrails are typically represented using simplified models because the contrail-scale processes are sub-grid and can not be resolved. The contrail occurrence frequency and coverage is computed using criteria due to Appleman (1953) and Schumann (1996). For instance, the Federal Aviation Administration's System for assessing Aviation's Global Emissions (SAGE) provides the emission index of water and engine efficiency for a particular engine type and fuel along radar-detected aircraft trajectories (Klima and Waitz, 2006). The criteria are then used to predict the formation as well as persistence of contrails in a given region (Schrader, 1997). The criteria are applied in a GCM using local atmospheric data and all aircraft trajectories in a grid cell are modeled as linear contrails.

The local relative humidity in the UTLS (upper troposphere lower stratosphere) region predicted by inline or offline models themselves has large uncertainties. This contributes to a major source of uncertainty in contrail predictions, which require accurate prediction of ice supersaturation at the cruise altitudes. In this study our focus is not on the prediction of water vapor in the atmosphere, but rather, is on the calculation of contrail properties under given atmospheric conditions such as temperature and relative humidity.

Ponater et al. (2002) first provided a parameterization scheme for contrails in GCM. The advantage of parameterization is that the contrail RF is then sensitive to the local atmospheric conditions. Although improved models exist which use tailored versions of the criteria for specific aircraft (Schrader, 1997) and couple the contrail parameterization scheme with the cloud parameterization scheme (Ponater et al., 2002), recent studies indicate that the uncertainties in contrail RF from various models can differ by an order of magnitude (Marquart and Mayer, 2002). This can be partially attributed to uncertainties in atmospheric data and insufficient resolution of available data in a given region. Other factors are the inability of the contrail parameterizations to include effects of spreading (Minnis et al., 2004) and the difficulties in incorporating the effect of many physical parameters such as the engine type and ice nuclei size in complete detail. Due to the large grid sizes of GCM calculations, many physical details are empirically modeled or simply assumed. For example, non-spherical geometry of ice particles is accounted for by an empirical asymmetry parameter, and overlap between cloud layers is sometimes assumed to be maximum or random (Marquart and Mayer, 2002).

Studying contrails at higher resolutions than those allowed by GCM has the potential of taking into account many of these factors thereby improving the accuracy of predictions. Such

simulations provide much more detailed physical effects, e.g. plume dynamics, buoyancy effects, turbulence and fluid dynamical instabilities. The insights and numerical databases generated by the simulations would be useful in developing improved models for use in GCM. The remainder of this introduction provides an overview of contrail simulations at various scales and levels of accuracy, and identifies questions where high-fidelity simulations can be a valuable tool for finding answers.

Contrail simulations: Previous work

Perhaps the most important factor that generates the need for improved accuracy of contrail models is the scale disparity between the smallest resolved scales in a GCM and the contrails scales. The former can be as low as a 700 meters in vertical direction and as high as a few hundred kilometers in the horizontal (Ponater et al., 2002). The contrail plume processes take place on scales of the order of meters (Paoli et al., 2004; Lewellen and Lewellen, 2001). Therefore box models are used to treat plume mixing, early particle size changes, and chemistry (Kraabol et al., 2000). Since such models do not account for the detailed microphysics and heterogeneous chemistry, coupled trajectory box models are required which treat both plume and background atmospheric conditions in separate but coupled boxes (Meilinger et al., 2005). But box models do not take into account the fluid dynamical details (e.g. plume entrainment by turbulent motion) which can be important for ice growth characteristics (e.g. Meilinger, et al., 2005).

Two- or three- dimensional simulations of contrails can provide a much more detailed prediction of contrail properties because the simulations involve fewer modeling assumptions and more physical effects are directly simulated. For instance, the entrainment, detrainment, and mixing of the jet plume into the ambient air have been studied using parabolized Navier-Stokes simulations (Quackenbush et al., 1996). This study investigates the dilution of the plume passive scalar and temperature, and qualitative dependence of plume dispersion on buoyancy of the jet. Such details are thought to be important inputs for regional/global contrail calculations, and need to be studied in more depth. The current study performed a parametric study of two dimensional plumes in aircraft wakes to find the fundamental mechanism behind plume entrainment (Shirgaonkar and Lele, Phys. Fluids, 2007).

Lower-order models that track the evolution of thermodynamic properties (supersaturation, temperature) in air parcels following a set of given trajectories can have detailed chemistry and microphysics (Karcher, 1994; Brown et al., 1996) and are computationally inexpensive. However, they involve many simplifying assumptions regarding the three-dimensional flow phenomena occurring in an actual contrail. For example, the effect of turbulent transport is incorporated by using an exchange coefficient, ϵ , which is only a function of the downstream distance (Karcher, 1994), and the loss of ice crystals due to sublimation is sometimes tackled using a tunable parameter (Sussman and Gierens, 2001). It is not known which of the early-stage physical effects would impact the global effect of contrails to a degree that they must be modeled directly into contrail calculations, as opposed to indirectly modeling them in a tailored way for a particular set of conditions. High-resolution three-dimensional simulations would help us get closer to knowing this, although it will take sustained research programs to generate sufficient knowledge base for a variety of atmospheric and aircraft conditions.

Because of the different characteristics of various regimes of contrail life, the numerical simulations are carried out at different levels of modeling. Several studies have been devoted to the exhaust species and particulate evolution including observations (Schumann et al. 1995), and simulations (Durbeck and Gerz, 1995) but there are relatively few high-resolution contrails simulation studies. Two-dimensional studies of contrails including both the jet and vortex regimes have been done by Sussman and Gierens (1999) where their interest was to investigate the role of the secondary wake on contrail growth. Two-dimensional large eddy simulations of Gierens (1996) study contrails of age 100 s and later, and do not treat the initial duration of the vortex stage which is important for contrail predictions. More advanced three-dimensional simulations by (Chlond, 1998) investigate contrails in the late dispersion phase (>1000s). Obtaining initial conditions for such longer time simulations is a necessary task and LES has recently emerged as a potential promising approach for it. The detailed simulations of Lewellen and Lewellen (2001) consist of a limited parametric study of contrails at a few sets of atmospheric and aircraft conditions. The range of parameters covered is still not sufficient to infer which physical parameters are important to the long-term contrail growth. Ambient relative humidity, as expected, emerges as one of the most crucial parameters affecting contrail growth (Lewellen and Lewellen, 2001) as we later confirm in this study. More physical processes should be investigated in such simulations.

The very early jet and vortex stages have been simulated using LES by Paoli et al., (2004) to study the flow physics and thermodynamics in the first 3s of contrail evolution. It is highly desirable to extend the time duration of contrail LES to include the jet, vortex, and dispersion regimes. Furthermore, a parametric study at different aircraft and ambient conditions is necessary to obtain useful information about contrail sensitivity to various parameters. The main objective of the current study is to provide such a parametric study for the jet and vortex regimes.

Objective

Our research focuses on highly resolved simulations of contrails of a typical subsonic transport aircraft with an aim to understand the sensitivities of the contrail evolution to various atmospheric conditions and aircraft parameters. The specific question this research effort hopes to address is how the amount of ice and its size distribution in aircraft contrails vary with the atmospheric relative humidity and temperature, and on aircraft engine parameters. The specific elements are:

1. Study the interaction between the jet exhaust plume and the vortex wake using large eddy simulation (LES) with a focus on the dispersal of condensed species and particles which may act as nucleation sites for ice-crystal growth in contrails.
2. Use Lagrangian modeling with ice-microphysics models for a large number of representative particles (10^5 to 10^6) in the turbulent wake-vortex flow fields (computed with LES) to study the properties of ice (size distribution, ice content, and optical depth) in contrails.
3. Conduct a collaborative assessment of different ice microphysics models and the contrail simulations at various levels of details (microphysics, passive tracer, contrail).

4. Study the impact of the atmospheric variables (local temperature and relative humidity) and engine parameters (ice nuclei number density and size) on the properties of the contrail ice particles in the intermediate to late stage of the vortex-wake.

Research Approach

The approach taken uses Large Eddy Simulations (LES) of the vortex-wake and turbulent exhaust jet along with Lagrangian tracking of ice particles. The first stage of the simulation uses a domain which is 4 and 5 wingspans wide in the directions transverse to the flight direction, respectively. The domain is one wingspan long in the flight direction, is stationary, and the aircraft cruises through it. The simulations begin 1 second after the aircraft passage. The simulations are capable of capturing the initial roll up of the wing-wake. In the first stage the simulations are intended to cover the contrail evolution from 1 second through 20 seconds downstream of the aircraft (see figure 12.1).

The Boeing 767 aircraft is chosen for the simulations at the cruise altitude of 10.5km. Atmospheric temperature and pressure corresponding to the U.S. standard atmosphere at the cruise altitude are used. Different values of ambient RHI are used. The total number of ice nuclei is based on an effective Emission Index (EI) of 10^{15} particles/kg-fuel, fuel flow rate of 0.685 kg/s/engine, and wingspan of 47.24 m. The initial data used vorticity, temperature and scalar fields provided by Boeing, generated from Reynolds Averaged Navier Stokes (RANS) simulations at Boeing.

Subsequent to the development of LES methodology and computer code, we performed comparison of passive tracer and ice microphysics between Stanford, Aerodyne and Boeing. We also simulated early-stage contrails (i.e. evolution up to 20 secs.) for various atmospheric conditions. Properties of the contrails predicted for a baseline atmospheric condition were also compared with predictions of a Boeing-WVU code (conducted by Boeing). A detailed report on the results from the early stage contrail evolution is available (see Shirgaonkar & Lele, 2007, TF Report No. 100). As a second phase of the LES study a small number of selected cases were continued to predict the contrail evolution up to 2 mins. The longer term contrail evolution required some further development of the code. In the following the principal results from this project will be given, including some highlights from the code intercomparisons.

Details of the mathematical model used to represent the contrail dynamics and the numerical algorithms used to solve these equations are given in Shirgaonkar & Lele, 2007, TF Report No. 100, hereafter referred as SL07. It solves the fluid dynamic and thermodynamic fields coupled by an extended Boussinesq approximation using high-order spectral-like finite-difference schemes. The ice-microphysics model uses a hybrid Eulerian-Lagrangian scheme where a large number of representative ice particles are treated in a Lagrangian fashion; their motion depends on the local fluid velocity and their thermodynamic evolution depends on the local relative humidity. When the ice particle is in local region where the air parcel is supersaturated with respect to ice its radius grows by condensation of the water vapor. The local air parcel loses vapor phase water in this way and gains the latent heat released. Liquid phase water is not explicitly treated.

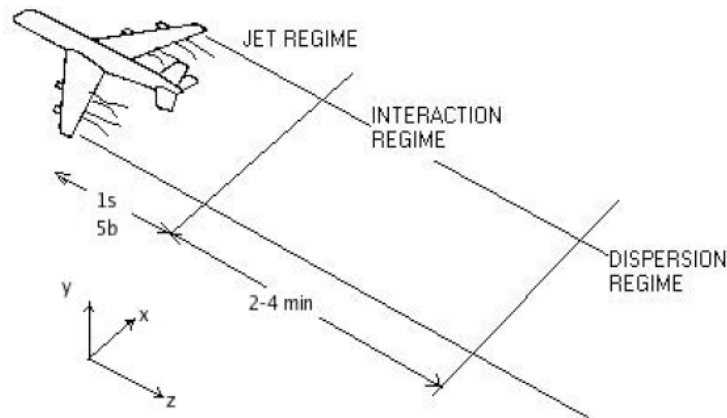


Figure 12.1. Schematic of wake-jet development regimes behind a transport aircraft. The wingspan is denoted by b .

Results:

1. *Intercomparison of ice microphysical models*

The performance of the Stanford Lagrangian microphysics model was compared with the predictions obtained by the Boeing and Aerodyne models for the same conditions using box model calculations. A set of 14 test cases (see Table 1) designed by Boeing spanning a broad range of atmospheric conditions (such as different relative humidity and temperature) and initial contrail properties (such as size, size distribution, and number density of ice particles) typical of a large subsonic aircraft at cruise was used for systematic comparison of the models. Boeing lead this subtask, and the overall comparison was good in terms of both qualitative and quantitative agreement. The intercomparison ensured that same (or nearly the same) thermo-physical properties were used by all models. The remaining differences among the models are largely understood, and steps have been identified to update the Stanford model to treat repeated growth of ice on contrail processed ice nuclei which could be important for long-term evolution of the contrails.

The test cases targeted the following factors affecting the contrail growth:

1. Atmospheric temperature
2. Relative humidity (RHI)
3. Initial ice nucleation particle size, size distribution and concentration
4. Kelvin effect (i.e. change in saturation pressure based on particle size)
5. Cyclic (temporal) changes in temperature

Run #	Temp (K)	Press (hPa)	RHi	Initial condition	Run time (sec)	Output interval (sec)	Rationale
1	220	240	110%	400 particles/cc r=0.5 microns	300	1	base
2	240	240	110%	400 particles/cc r=0.5 microns	300	1	Sensitivity to ambient temperature (water content)
3	200	240	110%	400 particles/cc r=0.5 microns	300	1	Sensitivity to ambient temperature (water content)
4	220	240	110%	400 particles/cc r=1 microns	300	1	Sensitivity to initial ice nuclei input
5	220	240	110%	50 particles/cc r=1 micron	300	1	Sensitivity to initial ice nuclei input
6	220	240	100%	400 particles/cc r=0.5 microns	300	1	Testing Kelvin effect
7	220	240	100%	3200 particles/cc r=0.5 microns	300	1	Testing Kelvin effect
8	220	240	100%	3200 particles/cc r=0.25 microns	300	1	Testing Kelvin effect
9	220	240	80%	400 particles/cc r=0.5 microns	300	1	Testing evaporation
10	220	240	130%	400 particles/cc r=0.5 microns	300	1	Testing large growth
11	$T=220K+0.02K \cdot \text{time in sec}$	240	110%	400 particles/cc r=0.5 microns	300	1	Test of temperature change due to parcel subsidence with constant H2O mixing ratio
12	$T=220K-2K \cdot \sin(2\pi \cdot \text{time in seconds} / 60)$	240	110%	400 particles/cc r=0.5 microns	300	1	Test of temperature response to growth/evaporation cycles Checking H2O accommodation coefficient
13	220	240	110%	Alpha=1	300	1	

Table 1: Test cases used for box model intercomparison between Boeing, Stanford and Aerodyne models. Boeing designed these cases and led the intercomparisons.

This allowed us to compare the models (within the setting of box calculations) for conditions representative of warm and cold contrails, sub-saturated, saturated and supersaturated ambient conditions (with respect to ice), rapidly evaporating contrails, and for contrails with Kelvin effect and warming effect due to subsidence. Results from the baseline case (Scenario #1) are shown in Figure 12.2. Note the rather close correspondence between the three models. In this case the ambient RHI is 110%. For RHI closer to 100%, larger quantitative differences between the models are observed but the trends are similar. The range of atmospheric conditions included in the test cases allowed some degree of confidence that the microphysical evolutions predicted by these models are physically similar.

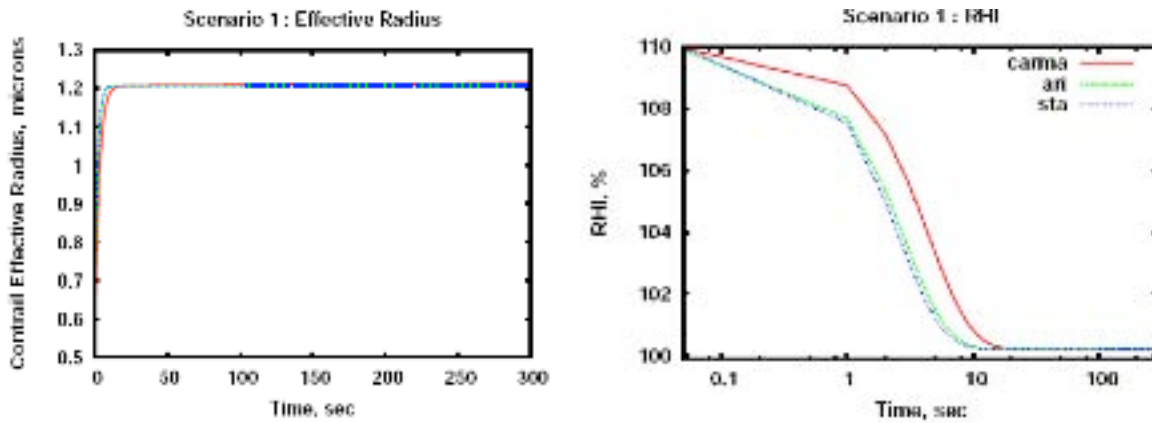


Figure 12.2: Contrail effective radius and relative humidity from box model calculations for the baseline case. carma: Boeing, ari: Aerodyne, sta: Stanford

2. Tracer LES comparison

We conducted parallel three-dimensional LES simulations at Stanford for initial conditions provided by Boeing. An independent simulation was conducted at Boeing using the Boeing-WVU code for matching conditions. Both models use different numerical schemes, and the comparison was aimed at understanding the differences between the two models. The Stanford contrail model uses Lagrangian microphysics, whereas the Boeing-WVU model uses Eulerian approach. Hence to compare these two approaches, we also conducted a comparison of the tracer LES results using both Lagrangian and Eulerian approaches (in the Stanford model). The results indicated that the difference between the two solutions is small. The tracer evolution predicted by the Lagrangian formulation is consistent with the Eulerian formulation. This establishes confidence that the water vapor field sampled by the Lagrangian particles in Stanford's ice-microphysics model is consistent with that which would be sampled by a pure Eulerian microphysical model (as in the Boeing-WVU code). Illustrative plots from this comparison are shown in Figure 12.3.

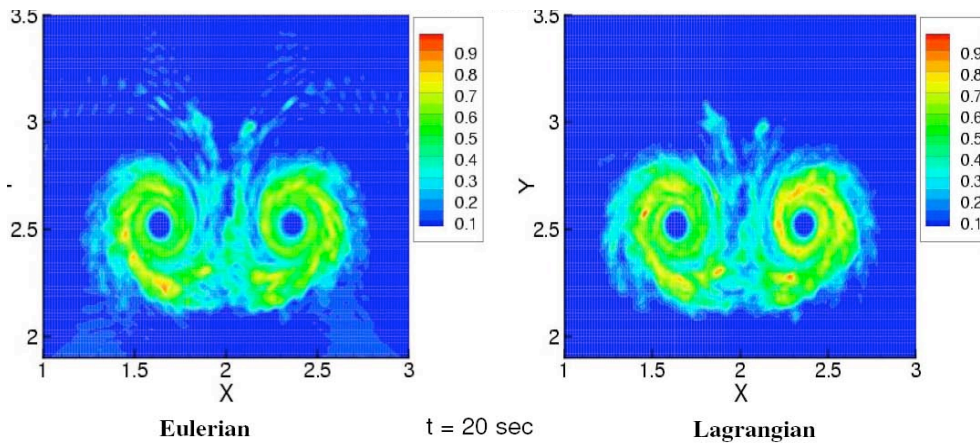


Figure 12.3. Tracer LES comparison using the Stanford code

As an additional step we also conducted an intercomparison of tracer fields with Boeing-WVU and Stanford LES solutions. Figure 12.4 shows the qualitative agreement between the two results. We have also conducted quantitative comparison in terms of vorticity and scalar line plots along the vortex centerlines. It showed good agreement between the two models. On the basis of these comparisons, we have confidence that the two LES codes predict very similar flow evolution when they start from nominally the same initial condition. It must be stressed that the initial condition is not exactly the same. The mean state is the same for the two codes but they each have their own way of initializing turbulent fluctuations. The method used in the Stanford LES code is described in detail in SL 07. The method used by Boeing for this is not known to us. Given these differences the comparison shown in figure 12.4 is a significant reassurance that the two models predict very similar tracer evolution.

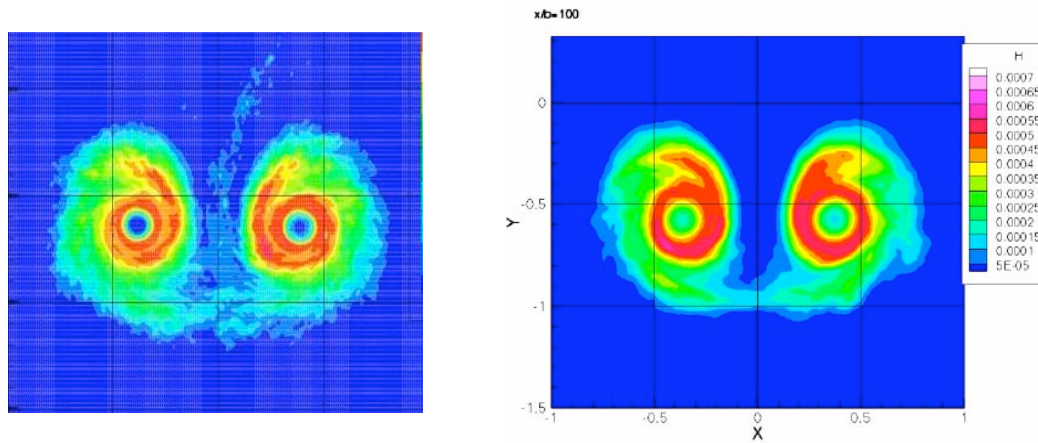


Figure 12.4. Tracer contours comparison between Stanford (left) and Boeing-WVU LES (right) at 20 sec. Axes ranges and contour levels are matched.

3. *Contrail sensitivity study*

The numerical tools developed for contrail LES were extensively validated using several test cases. These details are not reported here and can be found in SL07. Subsequently we conducted LES simulations for the first 20 seconds of contrail growth for a set of atmospheric conditions. The baseline case corresponds to 110% ambient RH_i at ambient temperature 218.8K, atmospheric lapse rate 2.5K/km, and ice nuclei (IN) number density 10^{15} #/kg(fuel). Figure 12.5 shows sample results for ice distribution in the early contrail. In all simulations reported in this report, the particle size remains small (less than 2 microns). Sedimentation of particles is neglected because it is expected to be small in the early stage of contrail evolution. Also, ambient turbulence and wind shear are not taken into consideration.

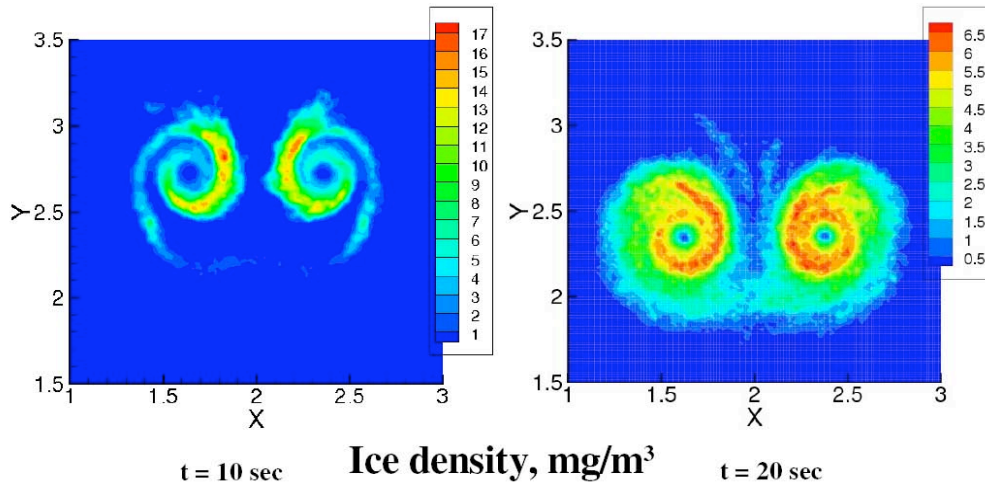


Figure 12.5. Ice density contours in early contrail, averaged in the flight direction

We carried out several simulations to study the effect of ambient RH_i and temperature, ice nuclei number density and initial ice particle size, and jet turbulence. These cases are summarized in Table 12.1. It should be noted that a larger parametric space will need to be covered to draw conclusions for the entire range of atmospheric conditions over which contrails are observed, but this is beyond the scope of the current study and the present representative range of atmospheric parameters is chosen for a parametric study.

Case	Ambient Temperature T_{amb}, K	Relative Humidity $RHi, \%$	Number of Ice Nuclei $N_p, \#/m$	Initial ice particle radius $r_{p0}, \mu m$	Turbulence seeded
A1	220	110	5.787×10^{12}	0.1	Yes
A2	220	130	5.787×10^{12}	0.1	Yes
A3	220	90	5.787×10^{12}	0.1	Yes
B2	200	110	5.787×10^{12}	0.1	Yes
B3	240	110	5.787×10^{12}	0.1	Yes
C2	220	110	2.894×10^{12}	0.1	Yes
C3	220	110	1.447×10^{12}	0.1	Yes
E2	220	110	5.787×10^{12}	0.05	Yes
E3	220	110	5.787×10^{12}	0.2	Yes
T2	220	110	5.787×10^{12}	0.1	No

Turbulence

Table 12.1. Simulation cases highlighting variation of different effects. The initial conditions for all cases have constant ambient water vapor density over the entire domain which are different for different RHi. The initial vapor density is obtained by imposing the stipulated RHi value at the initial vertical location of the vortex wake, $y = 3$, hence the RHi varies with y . Over this ambient vapor density field, the additional water vapor coming from the exhaust jet is added. Also note that N_p denotes the total number of ice nuclei per meter of the contrail.

Note that the high ambient temperature case ($T_{amb} = 240 K$) should be interpreted with care. According to the Appleman Criterion (Appleman, 1953), such warm atmosphere will not allow the formation of supersaturated liquid water, hence is not conducive to contrail formation. In the current code, the Appleman criterion is not directly imposed, but is meant to guide the interpretation of computational results for a particular set of atmospheric conditions. Thus, although the results for this warm atmosphere case indicate contrail formation, this is used only to display the sensitivity and should not be used at the stipulated ambient temperature because the Appleman Criterion disqualifies this temperature for contrail formation.

We compared the baseline case with simulations with higher (130%) and lower (90%) RHi, and with simulations for lower (200K) and higher (240K) ambient temperatures (T) to study the sensitivity of contrails. We found large impact of T and RHi on contrail growth. In particular, a rapid initial ice growth takes place in the first second, followed by the regime dominated by wake dynamics and turbulence (up to 5 seconds or so), followed by the Rhi-dominated stage beyond 8 seconds or so in the current simulations (Figure 12.6). Contrail at higher atmospheric temperature behaves very differently compared to those at lower temperatures (Figure 12.7). This is because the jet *absolute* humidity is not related to the ambient humidity, and is kept constant among different simulations. At higher ambient temperatures the effective relative humidity of the jet is lower, causing rapid ice particle loss due to evaporation.

In general, the particle size distribution remains qualitatively unchanged over the intermediate regime (1-5 sec) as seen from Figure 12.8, but the later, in the Rhi-dominated regime, it exhibits gradual spreading.

We also studied early contrails for two different ice nuclei (IN) number densities (2.89×10^{12} #/m in flight direction and 1.45×10^{12} #/m), in addition to the baseline case (5.79×10^{12} #/m). It was found that the higher IN number density caused greater depletion of water vapor from the atmosphere, hence faster particle number decay due to evaporation and smaller ice particles. Variations in the initial ice particle size from 0.05 to 0.2 microns, however, did not show much impact on the contrail growth in terms of ice water content or surface area.

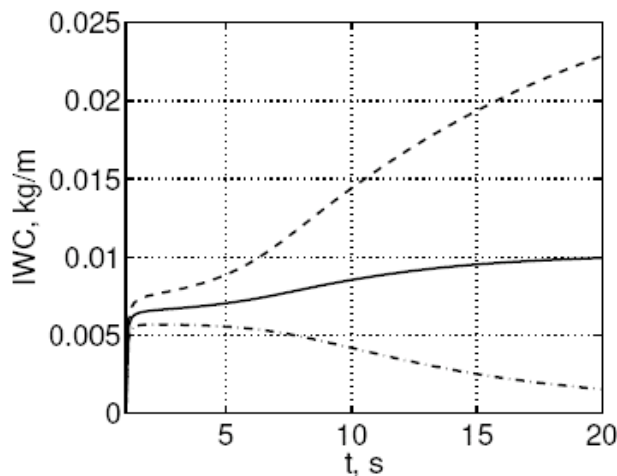


Figure 12.6. Ice water content for different RHi values but constant T. ___: 110%, ---: 130%, -.-: 90%

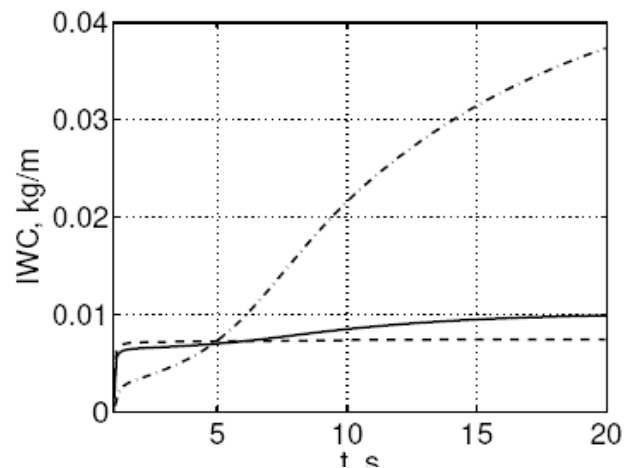


Figure 12.7. Ice water content with for different ambient temperatures but constant RHi. ___: 218.8K, ---: 200K, -.-: 240K

To assess the effect of variations in jet turbulence that is seeded into the initial conditions, two different ways to generate initial conditions were compared. The first way, which is used in the results described so far, uses the flow field at 5 wingspans provided by Boeing using its RANS simulations, seeds turbulent fluctuations on top of it, and uses the resultant data as the initial conditions for contrail LES. The other way is to allow the jet to evolve and become turbulent separately (in absence of aircraft wake and ice particles) so that realistic turbulence is developed, and then use this turbulent jet for contrail LES. Although the results from these two types of simulations show some basic differences, at 20-second duration the quantitative differences between them appear to be small (Figure 12.9).

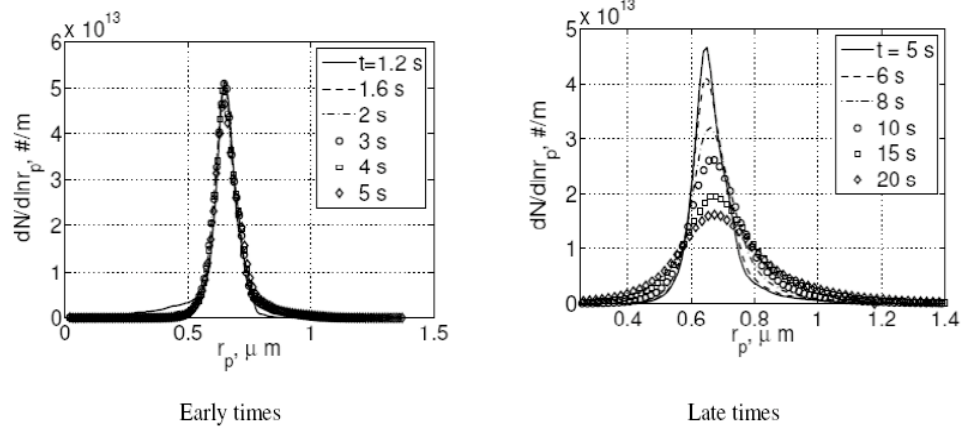


Figure 12.8. Plume-integrated ice particle size distribution for baseline case

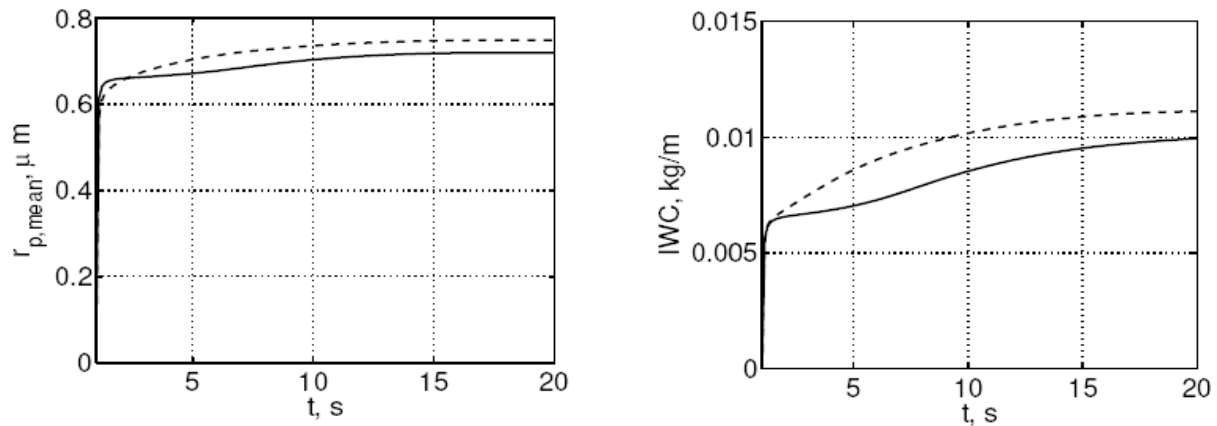


Figure 12.9. Effect of jet turbulence seeding on mean radius and ice water content for the baseline case using without (solid line) and with (dashed line) realistically developed jet turbulence. Left: mean ice particle radius, right: plume integrated ice content.

Since the use of computational particles as representative of collections of actual ice particles is central to the Lagrangian approach, it is important to assess the sensitivity to the number of computational particles (N_c) used (which is an input parameter). Results from two different simulations with 1 million and 0.25 million computational particles were found to be close. In particular, the particle size distribution is not adversely affected by N_c in the range considered (Figure 12.10). Figure 12.11 shows that the ice particle number density is also not affected very much by N_c in this range. This has only been verified for the initial 20 s duration for which the simulations were run. For longer time evolution, this may have to be verified separately.

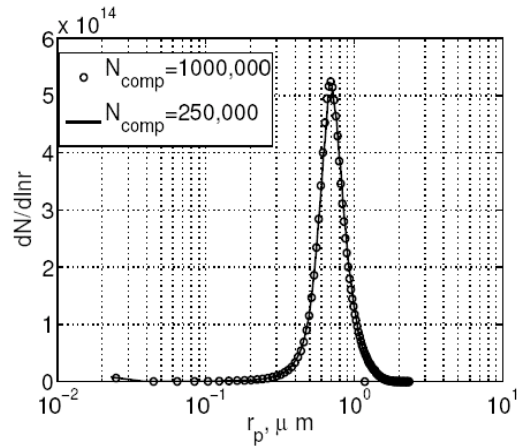


Figure 12.10. Plume-integrated ice particle size distribution at $t = 20$ sec.

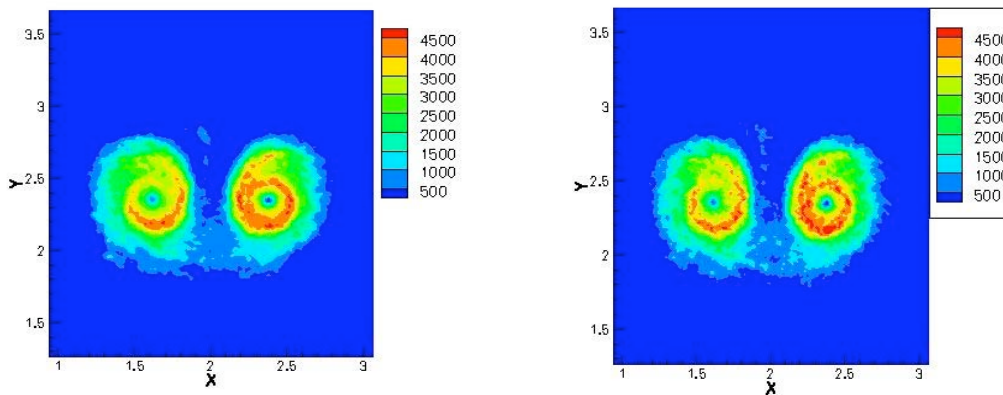


Figure 12.11. Ice particle number density in $\#/cc$ at $t = 20$ sec, averaged in the flight direction. Left: $N_c = 1000,000$; right: $N_c = 250,000$.

4. Contrail LES intercomparison with Boeing-WVU code

Contrail properties predicted by the Stanford LES code for the baseline case were compared in detail with predictions obtained by Boeing using the Boeing-WVU code. The baseline case corresponds to 110% ambient RH_i at ambient temperature 218.8K, atmospheric lapse rate 2.5 K/km (which is the rate of change of potential temperature with height) and ice nuclei (IN) number density 10^{15} $\#/kg(\text{fuel})$. These codes differ in the numerical algorithms used and have fundamentally different approaches for modeling the ice-microphysics. The Stanford code uses Lagrangian particle tracking for condensational ice growth combined with Eulerian calculations of fluid and thermodynamic variables, whereas the Boeing code uses binned microphysics (number density in each size bin is regarded as an Eulerian variable). As discussed in section 2 the tracer inter-comparison between these two codes showed the tracer predictions to be close with similar shapes in the distribution of the tracer with time and similar levels of dilution.

A comparison of the overall plume averaged ice properties up to 20 secs. is shown in Figure 12.12. Evidently both codes predict approximately the same amount of total ice mass, shown as ice water content (IWC) in Figure 12.12(a), as a function of time. There are, however, some differences especially at early times which might be related to the manner in which the two codes initialize the turbulence field. It was not possible to duplicate these exactly, since we do not have access to the Boeing-WVU code details. In Figure 12.12(b) the size distribution of the contrail ice at $t=20$ sec are compared. It is observed that the Stanford code predicts a smaller number of the very large ice particles (particle radius $> 2.0 \mu\text{m}$ and a significantly larger number of ice particles in the size range around $0.5 \mu\text{m}$ while predicting approximately the same amount to total ice mass.

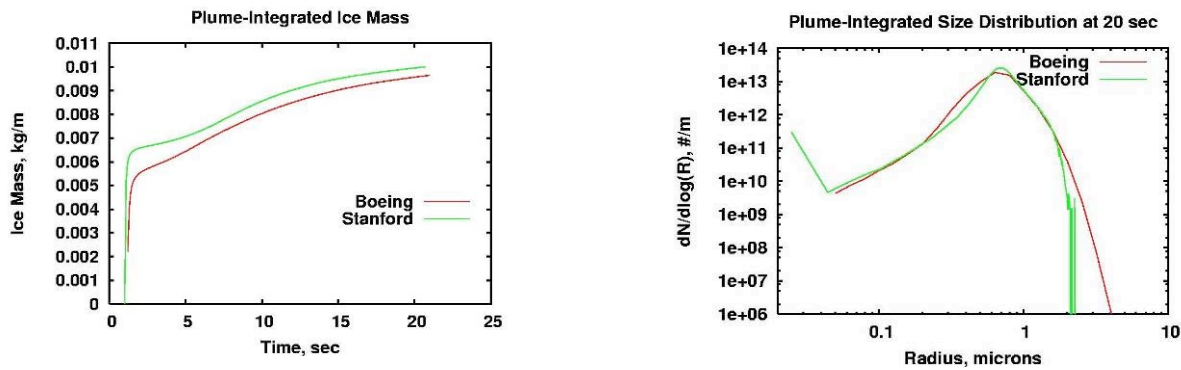


Figure 12.12a and 12.12b, Comparison of overall contrail ice properties.

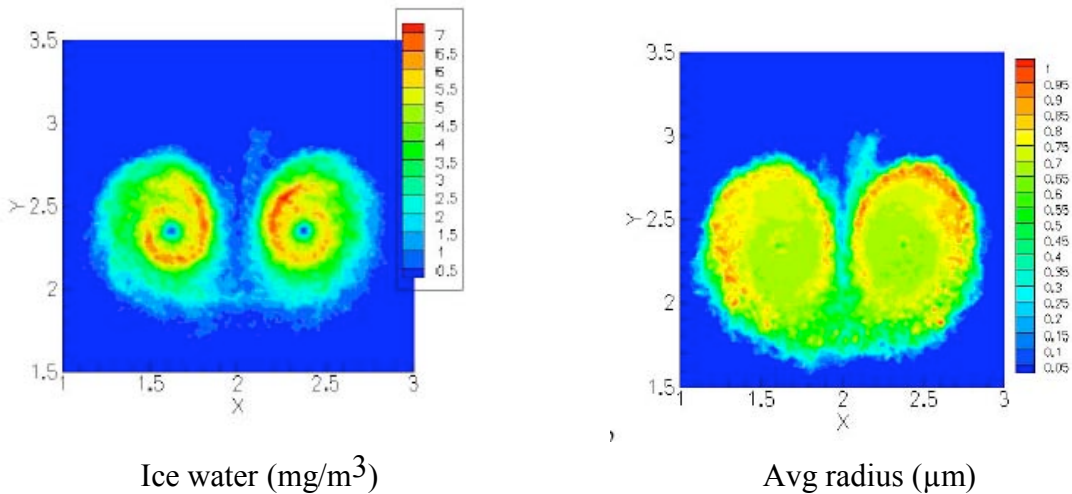


Figure 12.13: Ice density and Average radius contours from Stanford code.

A more detailed comparison of the predictions of the two codes can be seen by comparing Figure 12.13 (Stanford code) and Figure 12.14 (Boeing-WVU code). Figure 12.13 shows the predicted distribution of ice water and average particle radius for the Stanford code. The same quantities for the Boeing-WVU code are plotted in Figure 12.14. Evidently, while the distribution of ice mass is quite similar, the

predicted average particle radius is quite different. The Boeing-WVU model predicts large regions around the vortex-pair with large ice particles. These differences could imply significant differences in the optical properties of the contrails predicted by the two models, but since such a comparison is more instructive at the intermediate- to late-stages of contrail evolution we defer further comments on the intercomparison for future when data over a longer time horizon will be compared. It should, however, be noted that studies of the numerical convergence of the solution with respect to the Eulerian grid spacing and with respect to the number of Lagrangian particles tracked were conducted (see SL07) and the results did not indicate any sign of lack of convergence. It appears that the difference observed here may be due to a) the differences in the microphysical models used and b) due to difference in the manner in which turbulent fluctuations are specified at the start of the calculation. As discussed earlier in the context of figure 12.9, the initial turbulence seeding (within Stanford LES code) was found to cause some difference in the mean ice particle radius and total ice mass but these differences are too small to explain the qualitative difference in the distribution of average ice particle radius seen by comparing figure 12.13 and 12.14. The differences in the way ice-microphysical evolution is treated in the two codes is therefore expected to play a large role.

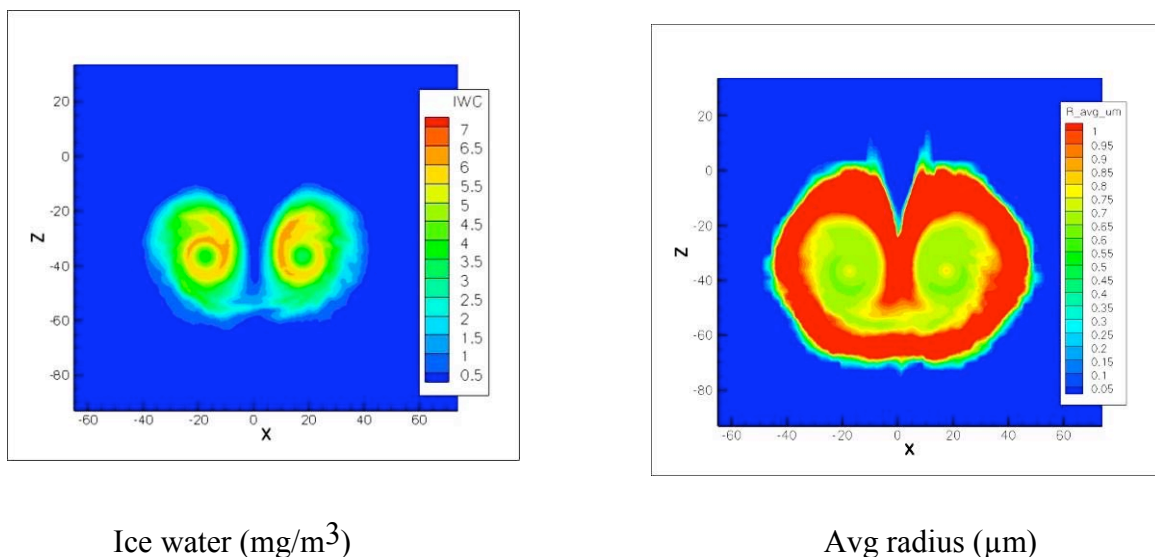


Figure 12.14: Ice density and Average radius contours from Boeing-WVU code

5. Contrail Simulations over 2 minute time horizon

5.1 Simulation methodology

The simulations are conducted in two stages. In the first stage the simulations are intended to cover the contrail evolution from 1 second through 20 seconds downstream of the aircraft. This can be achieved with a modest sized domain which is $1\ b$ long along the flight direction and $4\ b$ wide and $5\ b$ in the vertical direction, taking b as the wingspan. Contrail evolution under a variety of atmospheric conditions was studied in this initial phase. The second phase of the simulation covers up to 2 minutes of evolution and requires significantly larger domains ($10\ b$ in the flight direction, and $4\ b$ wide and $10\ b$ tall). The relatively finer scale at which the jet plume is initially rolled up by the aircraft vortex wake requires a fine spatial resolution. This roll up phase (1 through 20 secs. of evolution) is captured with a suitably fine grid resolution in the first stage calculations. The calculation starts with a fine mesh which is isotropic in directions transverse to the flight direction and with 20 grid points across the initial vortex core. This level of resolution was found to be sufficiently accurate in grid resolution tests reported in SL07. Once the jet roll up is complete, it becomes possible to reduce the grid resolution. The data from the fine mesh calculations are interpolated to a coarser mesh at the time of 10 sec and the run continued on the coarse mesh which covers the same spatial domain but with grid spacing increased to 2 times the fine grid value. This combination allows the early and intermediate stage of contrail evolution to be captured. A similar transfer of flow data to a much larger domain along with appropriate modeling of the atmospheric turbulence will be needed to achieve simulations of late stage contrails going beyond the 2 minute time horizon. This late stage of contrails was not studied in the present work.

The Boeing 767 aircraft is chosen for the simulations at the cruise altitude of 10.5km. Atmospheric temperature and pressure corresponding to the US standard atmosphere at the cruise altitude are used. Different values of ambient RHI are used. The total number of ice nuclei is based on an effective Emission Index (EI) of 10^{15} particles/kg-fuel, fuel flow rate of 0.685 kg/s/engine, and wing span of 47.24 m. The initial data used vorticity, temperature and scalar fields provided by Boeing, generated from Reynolds Averaged Navier Stokes (RANS) simulations at Boeing.

Fine mesh calculation with 256 by 640 by 640 points were run up to 15 sec. At $t = 10$ sec the data was interpolated to a coarser mesh of 128 by 320 by 320 points while maintaining the same physical domain. Comparison of the coarsened mesh calculation with the original finer mesh calculation over the 10-15 sec time window allowed the accuracy of the new calculation to be established. The coarsened mesh calculation was run up to $t = 120$ sec. A comparison of the fine-mesh results with those on the coarser mesh (see figure 12.15) established that reduced mesh resolution was sufficient for the extended calculation.

5.2 Simulated cases

We carried out three simulations to study the effect of ambient RHi on contrail growth, and to determine the contrail sensitivity to the nature of the ambient water vapor distribution – constant water vapor, or constant RHi. The simulations are listed in Table 12.2 below. In the following we discuss the trends shown by these simulations.

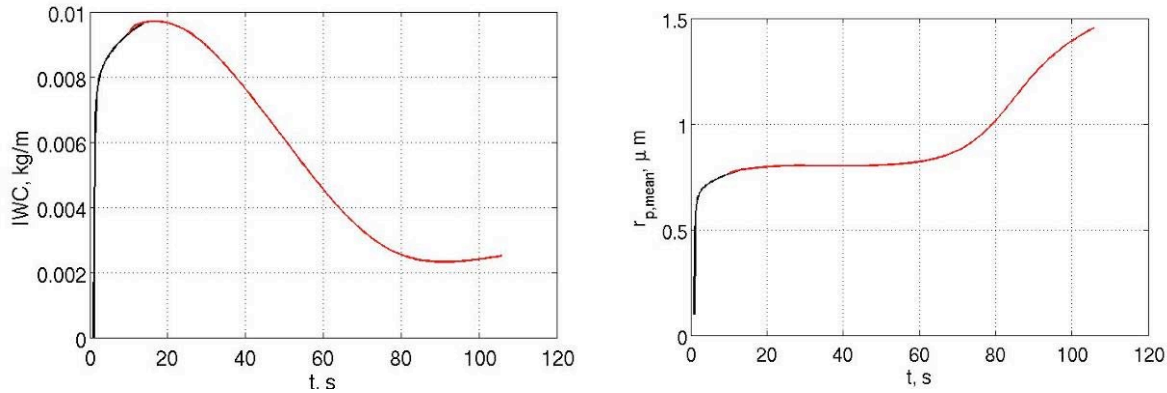


Figure 12.15 Comparison of overall contrail properties for fine mesh calculation in black lines up to $t = 15$ sec with coarser mesh calculations started at $t = 10$ sec. The data plotted is for the baseline case A1 in Table 1, for an ambient atmosphere with constant water vapor mixing and R_{Hi} of 110% at the flight altitude.

<i>Case</i>	<i>RHi at 10.5 km %</i>	<i>Ambient water vapor distribution</i>	<i>Initial Conditions</i>	<i>Comments</i>
1	110	Constant	Gaussian jet	
2 Baseline	110	Constant gradient	Boeing IC	Small RHi gradient Closest to Baseline
3	130	Constant gradient	Boeing IC	Small RHi gradient Closest to 130%

Table. 12.2. Summary of simulation cases on 2 minute duration

5.3 Evolution of Contrail structure

We will first discuss the overall evolution of the contrail for the baseline case with ambient $R_{Hi} = 110\%$ (case 2). The effect of ambient R_{Hi} will be discussed subsequently. Figure 12.16 shows the distribution of ice mass in the contrail at $t = 10, 30, 60,$ and 120 sec., respectively. The distribution of ice particle number density at the corresponding times is shown in Fig. 12.18. Evidently, the contrail develops a head-and-tail structure during the first minute of evolution. As discussed previously, in section 3, during the first 10-15 secs. of evolution the water vapor contained in the jet plume is stretched and rolled up around the descending vortex-pair. Condensation of water vapor on the ice nuclei in the jet plume forms the 'head' of the contrail which progressively descends. Not all of the ice particles are transported with the contrail 'head' and a wake region is formed. This wake region contains ice-particles which are not entrained into the 'head' region and those which are detrained due to buoyancy effects. The wake or 'tail' region stretches from the 'head' back to the original flight altitude. It is notable that the region with largest ice mass is located in the 'tail' while the largest ice-particle number density is within the 'head'. Several factors contribute to bring about this distinct spatial structure. Consider the distribution of average ice particle radius in the contrail shown in Fig. 12.20. The largest ice particles are found in the tail region while in the head region there is preponderance of smaller ice particles. This observation is

further supported by Fig 12.22 showing the ice particle size distribution. Contours of RHi and the temperature field are shown in figures 12.23 and 12.25, respectively. Note that the 'head' of the contrail is marked by RHi levels close to the saturation value and a region which is locally sub-saturated with respect to ice is observed in the interior of the vortex-wake. Ice particle growth occurs at the boundary between the wake and the exterior super-saturated air parcel.

Profiles of specific variables along the nominal symmetry plane of the contrail and cross-sectional profiles (spanwise cuts) provide additional insights regarding the structure of the contrail and its evolution. It is convenient to take these profiles at the symmetry plane of the contrail ($x = 2$). Profiles based on averaging the data in the flight direction were examined. It is seen from the RHi contour plots in Fig. 12.23 and the line plots (Fig. 12.27) that the vertical extent of the contrail increases progressively with time, and the contrail consists of the wake-vortex region, and a detrained region.

Figure 12.28 shows the changes in RHi and temperature along a horizontal line following the contrail head as it descends downward. It is seen that the RHi inside the contrail is not affected with time in this late regime, but the temperature of the contrail head (which is essentially the wake vortex) rises due to entrainment of warmer fluid from the ambience. The ice mass and particle radius, however, reduce with time in the head region. Since the overall IWC monotonically increases with time, this indicates that the ice content in the vortex wake becomes less and less in quantity, compared to the detrained plume, which is seen to dominate the IWC at late stages.

5.4 Effect of ambient RHi

We now discuss the ice mass contours for cases 2 and 3 (Fig. 12.16 and 12.17). It is seen that the ice mass distribution is qualitatively similar in both cases, with more ice growth exhibited by the higher RHi case. Observation of ice water content (IWC) (Fig. 12.16) and ice particle number density (Fig. 12.18) for case 2 show an interesting trend that the regions of high particle number density and high IWC are de-correlated. This means, small number of large particles contribute to a large amount of IWC near $y = 6$, (where the vertical coordinate y has been nondimensionalized by the wing span b). The large IWC found near $y = 3.5$ is caused by a large number of smaller ice particles trapped in the vortex wake. This is evident from the contour plots of ice particle radius (Fig. 12.20 and 12.21), and is further clear from the plots of particle size distribution in the upper half ($y > 5$) and the lower half ($y < 5$) in Fig. 12.22. The size distribution of ice particles along the mid-line of symmetry ($x = 2$) also corroborates this observation (Fig. 12.29). This figure also shows that the particle number density is relatively independent of the RHi in the late stage, and the ice mass distribution is governed almost exclusively by the particle size distribution.

Atmospheric properties also show a similar behavior in Fig. 12.29. The temperature distribution is relatively insensitive to the ambient RHi in the late stage. This may be primarily because, turbulent diffusion of thermal energy tends to diffuse away the small temperature differences caused by the latent heat deposition from the ice growth. At late times, the contrail is likely to have reached an equilibrium stage where the latent heat effect is small enough to be diffused quickly by turbulent diffusion. The RHi plot along the mid-line in Fig. 12.29 also show a similar trend, that inside the contrail "head," the RHi equilibrates around 100%, suggesting that the ice growth inside the contrail head adjusts to the incoming

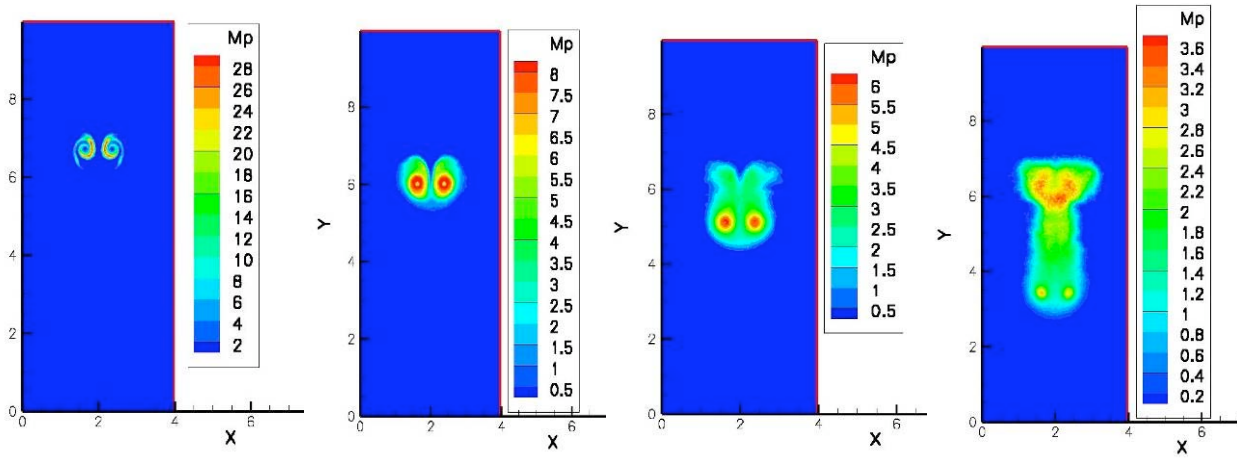


Fig. 12.16 Contours of ice mass in the contrail (in mg/m^3) for the baseline case ($\text{RH}_i=110\%$) at $t=10, 30, 60,$ and 120 s from left to right. At later times, an ice curtain is visible, consisting of the ice mass carried by the vortices and upwashed by buoyancy.

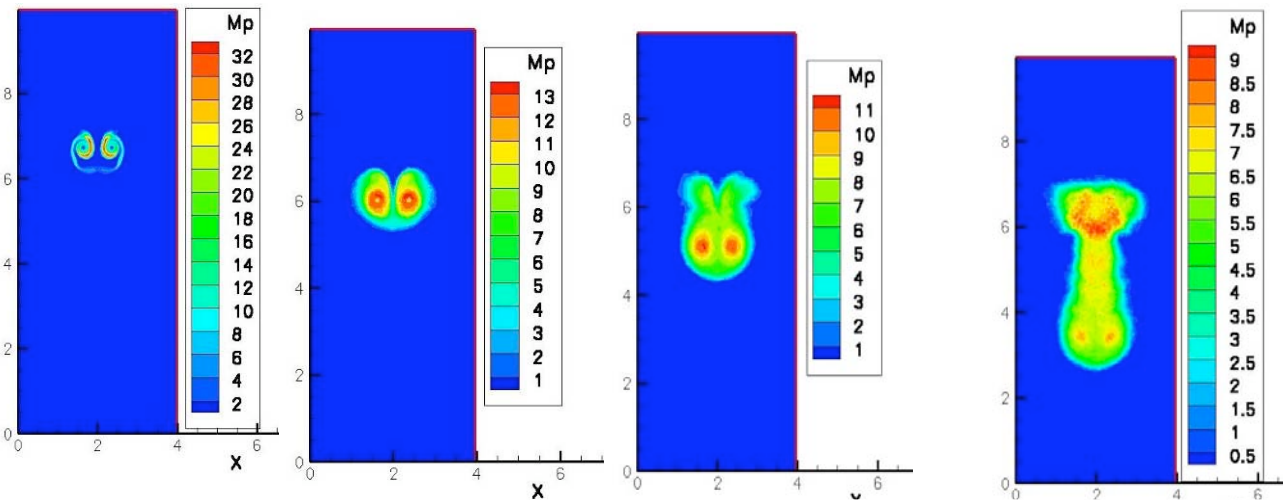


Fig. 12.17. Contours of ice mass in the contrail (in mg/m^3) for $\text{RH}_i=130\%$ case at $t=10, 30, 60,$ and 120 s. The qualitative behaviour is the same as with 110% , but ice mass density is higher.

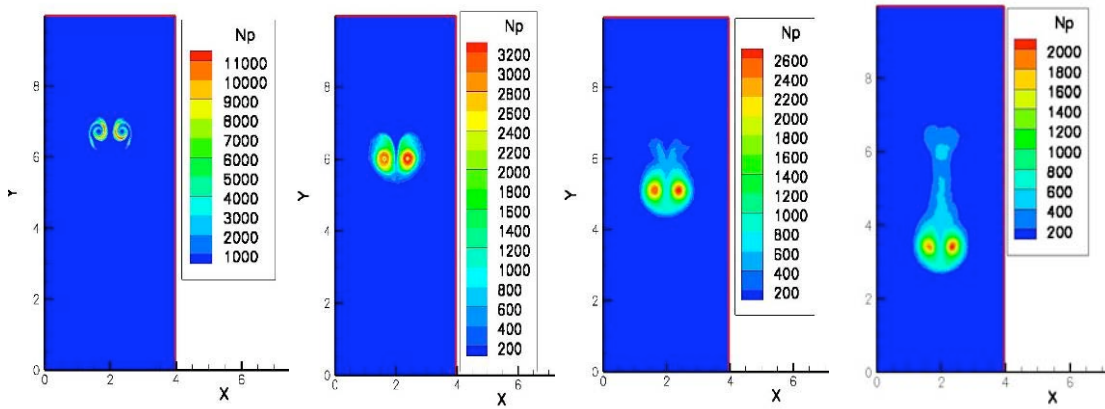


Fig. 12.18. Contours of ice nuclei number density in the contrail (in #/cc) for the baseline case at $t= 10, 30, 60,$ and 120 s. At late times (120 s), the majority of ice particles are carried downward by the vortices.

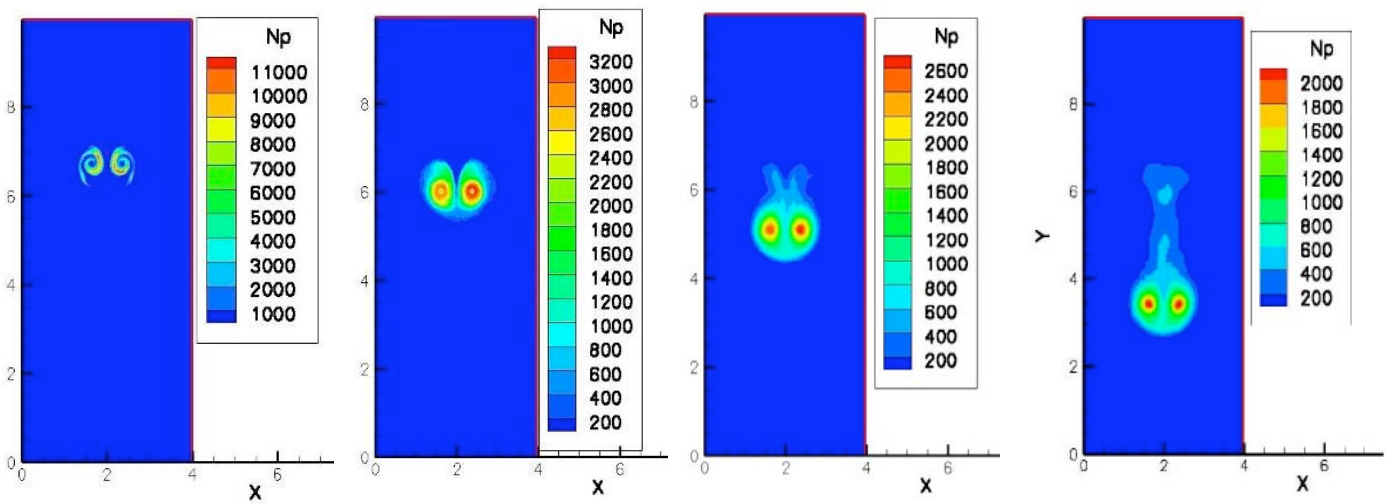


Fig. 12.19. Contours of ice nuclei number density in the contrail (in #/cc) for the $RH_i=130\%$ case at $t= 10, 30, 60,$ and 120 s.

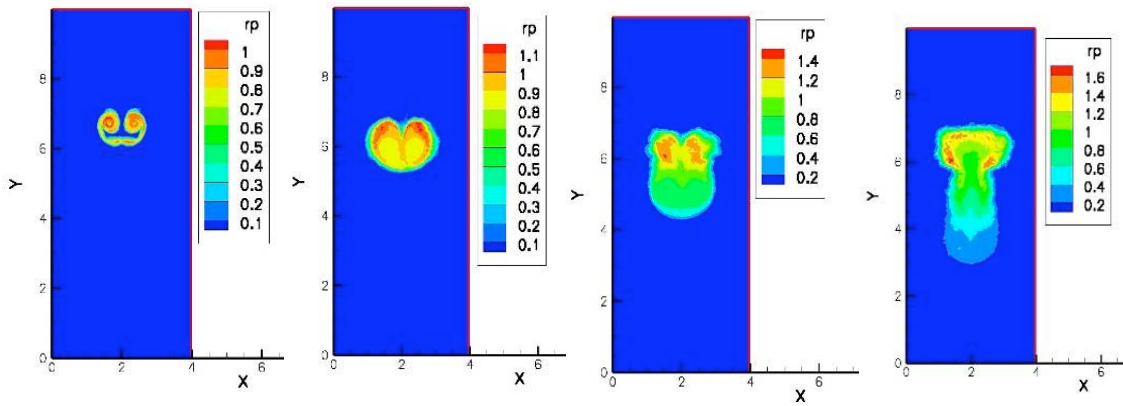


Fig. 12.20. Contours of average ice particle radius (in microns) in the contrail for the baseline case at $t=10, 30, 60,$ and 120 s. At late time (120 s), larger particles are concentrated in the detrained plume (near $y = 6.5$). Particles entrained in the vortices are smaller, but have higher number density as seen from Fig. 12.18.

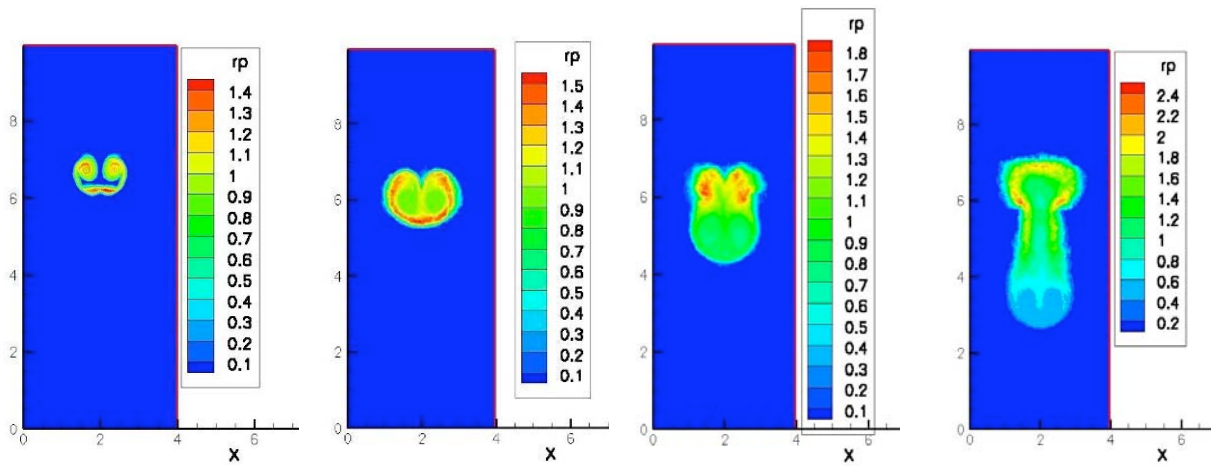


Fig. 12.21. Contours of average ice particle radius (in microns) in the contrail for the $RHi=130\%$ case at $t=10, 30, 60,$ and 120 s.

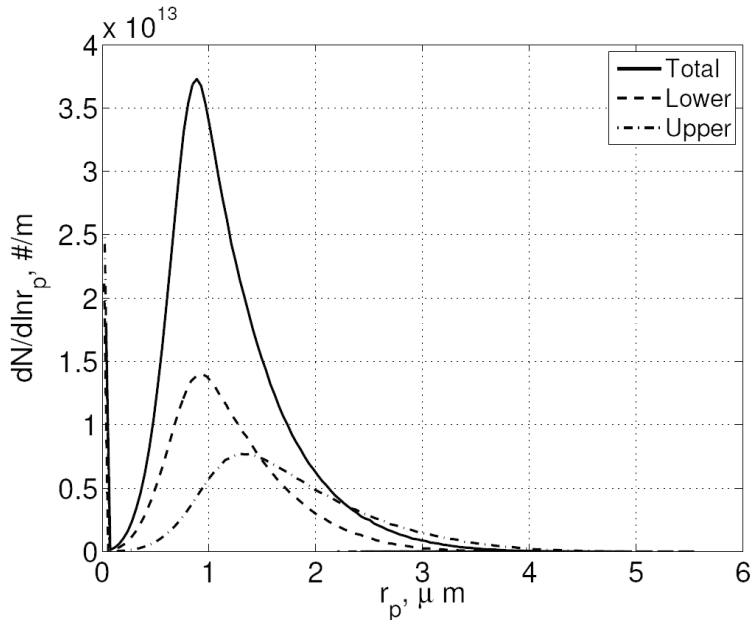


Fig. 12.22. Particle size distribution at 120 s for the total domain, upper half ($y > 5$), and lower half ($y < 5$), indicating that more larger particles are located in the detrained plume at late times.

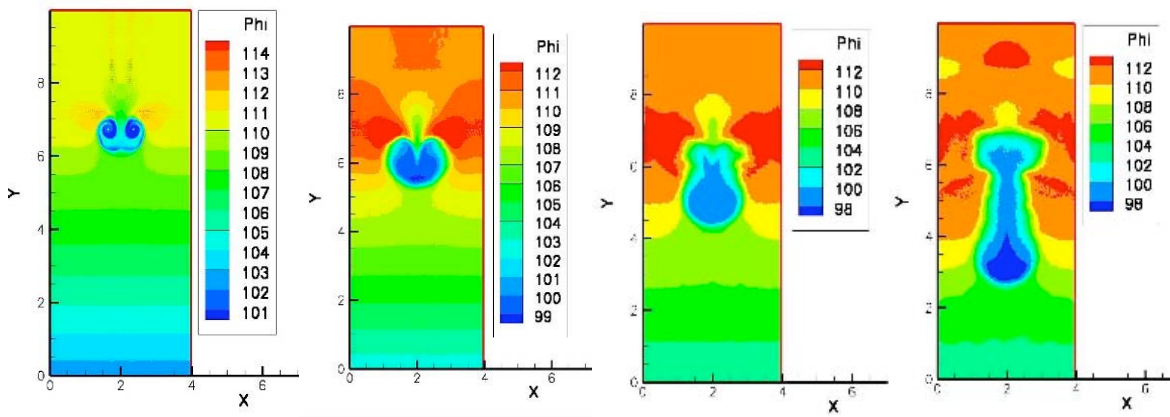


Fig. 12.23. Contours of RH_i in the contrail for the baseline case at $t = 10, 30, 60,$ and 120 s. Depletion effect causes local regions of low RH_i (blue), where large ice mass has formed (Fig. 12.16).

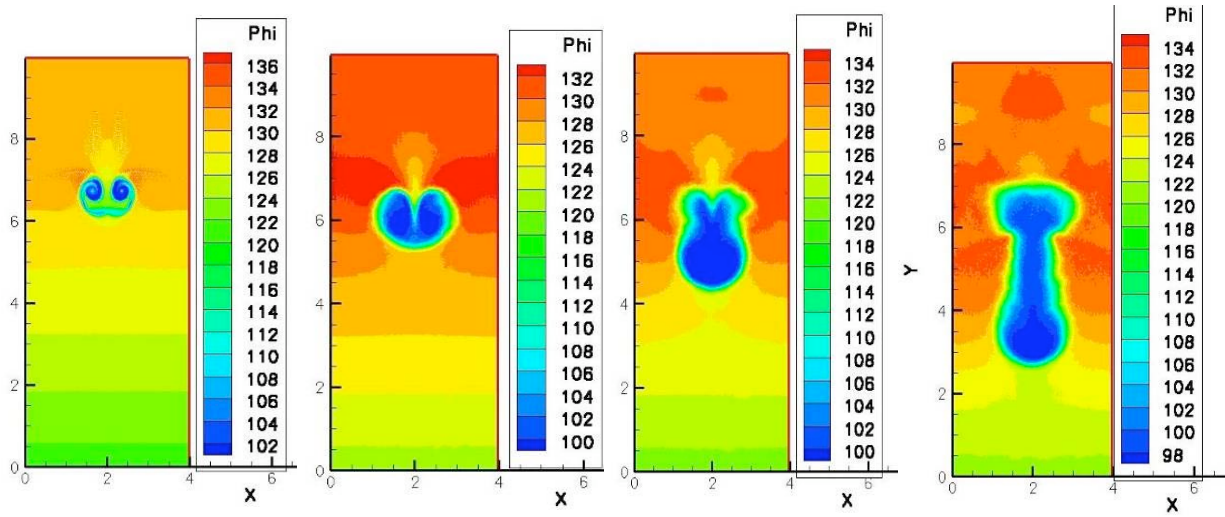


Fig. 12.24. Contours of RHi in the contrail for the RHi=130% case at t= 10, 30, 60, and 120 s.

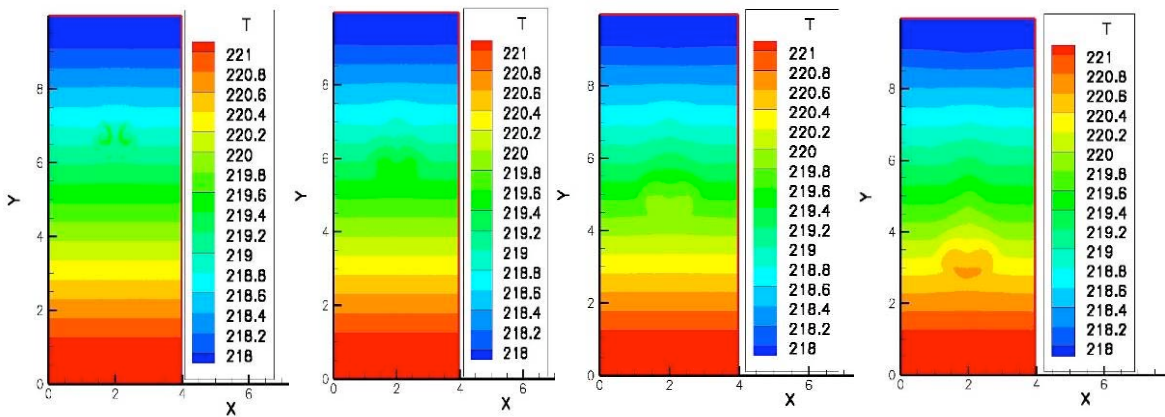


Fig. 12.25. Contours of average temperature (deg C) in the contrail for the baseline case at t= 10, 30, 60, and 120 s.

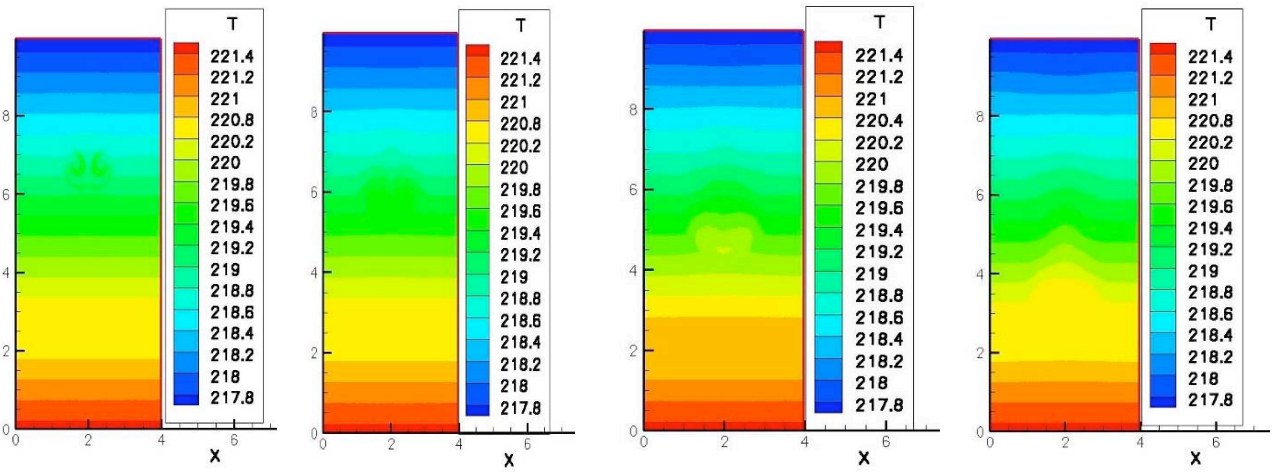


Fig. 12.26. Contours of average temperature (deg C) in the contrail for the $RH_i = 130\%$ case at $t = 10, 30, 60,$ and 120 s.

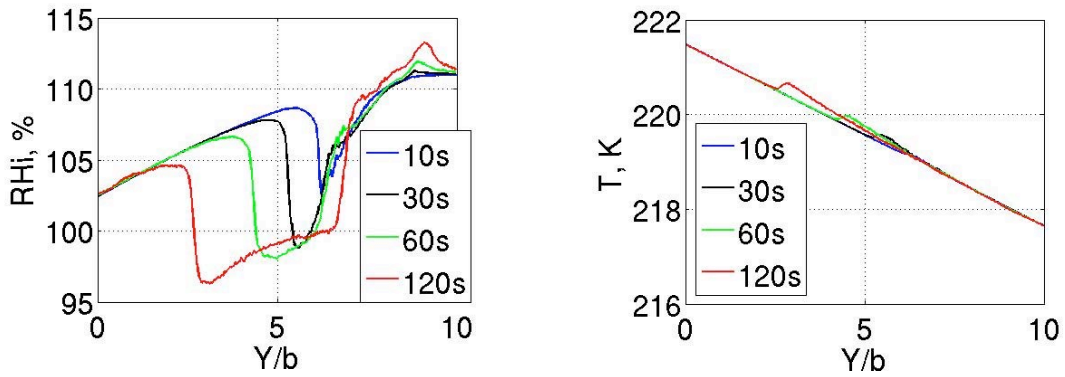


Fig. 12.27. Temporal evolution of RH_i and temperature along the vertical line of symmetry, $x = 2$. For Case 2.

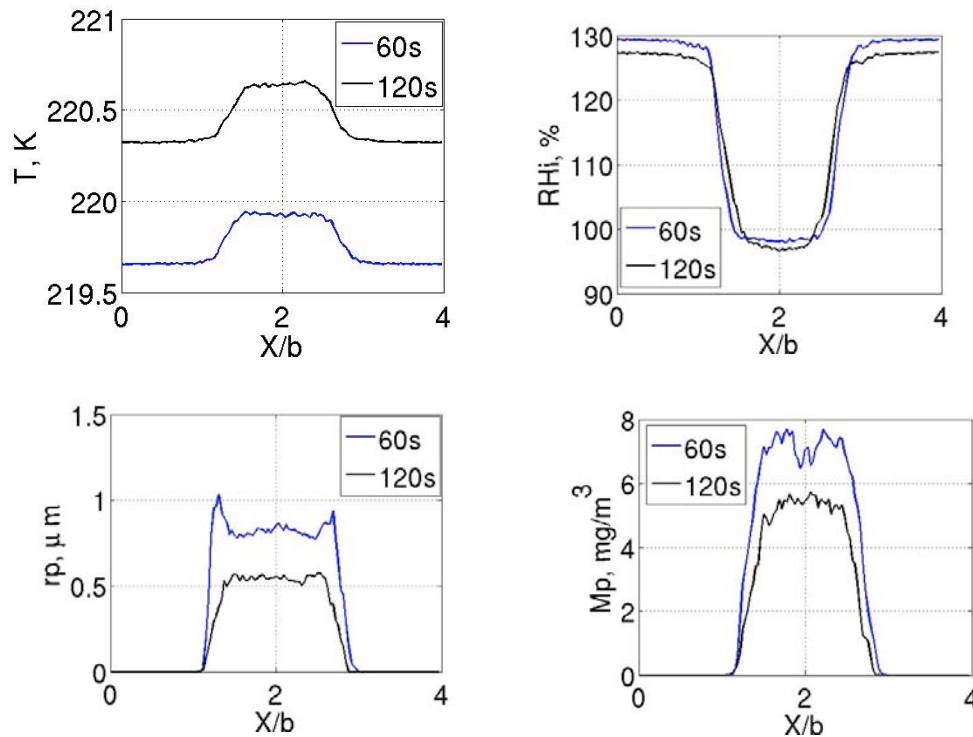


Fig. 12.28. Contrail properties along the lines $y = 3b$ (60 s) and $y = 4.72b$ (120 s) for the baseline case showing various properties following the contrail head as it descends down.

water vapor from the atmosphere (entrainment) in a way so as to attain a maximum growth allowed by the entrained water vapor. The entrainment region is distinguished by the rapid gradients of RH_i and temperature on the edge of the contrail (Fig. 12.29), outside which the atmospheric distribution prevails. Since the deposition process (which occurs on micrometer scales) is faster compared to flow evolution and turbulent diffusion (which occurs on centimeter scale), the ice particle size inside the contrail reaches the equilibrium quickly. This behavior is essentially the same as that observed in the early rapid growth of ice mass (Fig. 12.30) where the ice particles tend to reach an equilibrium with the excess water vapor in the jet by depleting the jet of its water vapor via the process of deposition. Behavior of integrated ice properties (total IWC, ice surface area, number density and particle radius) is shown in Fig. 12.30. Generally, larger particles are formed with higher humidity, and also higher RH_i causes higher IWC.

However, an apparent counter-intuitive trend is observed wherein higher RH_i causes a faster loss of smaller particles. This is primarily due to the depletion effect where the growth of ice locally depletes the ambient air of water vapor causing subsaturated regions. A secondary factor contributing to this trend is the addition of heat from depositing ice particle into the surrounding, which causes a reduction

in the local RHi around the growing ice particles. The depletion of local RHi is seen from the contours of RHi (Fig. 12.23 and 12.24) which show a lower RHi embedded in regions of higher RHi, and within those regions, a lower local RHi for higher ambient RHi case. The deposition of latent heat into the surrounding air, is evident from the temperature contours (Fig. 12.25 and 12.26) where the higher ice production rate (i.e. the RHi 130% case) shows higher temperature in the air surrounding the regions of ice. In this study we performed simulations over the first 20 seconds with first the latent heat coupling turned off, and then both latent heat and mass transfer turned off. The former showed a very small effect while the latter showed a substantial effect. This demonstrates that the dominant factor for this counterintuitive trend is the depletion of water vapor caused by local ice growth.

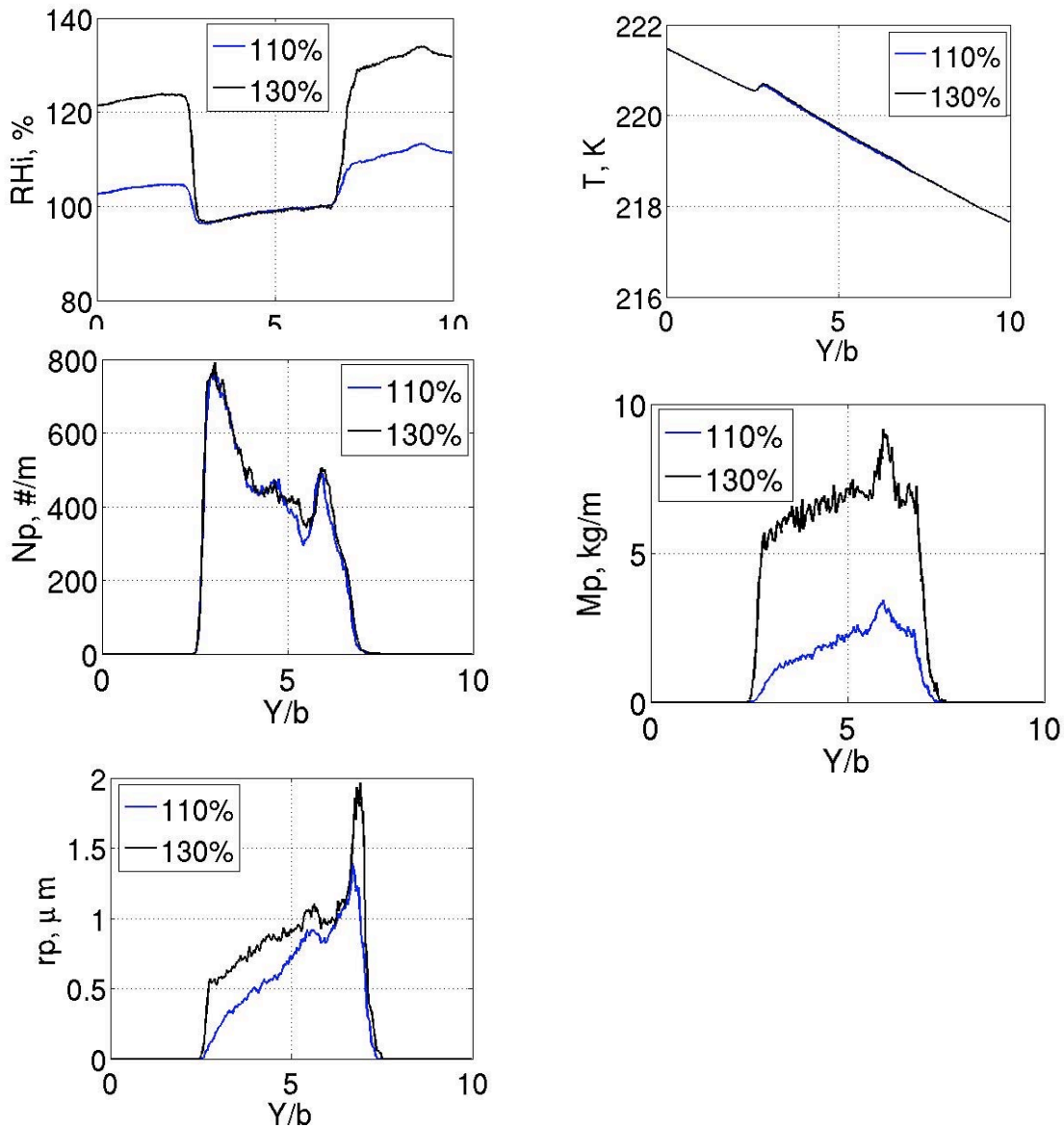


Fig. 12.29. Contrail properties along the line of symmetry ($x = 2$).

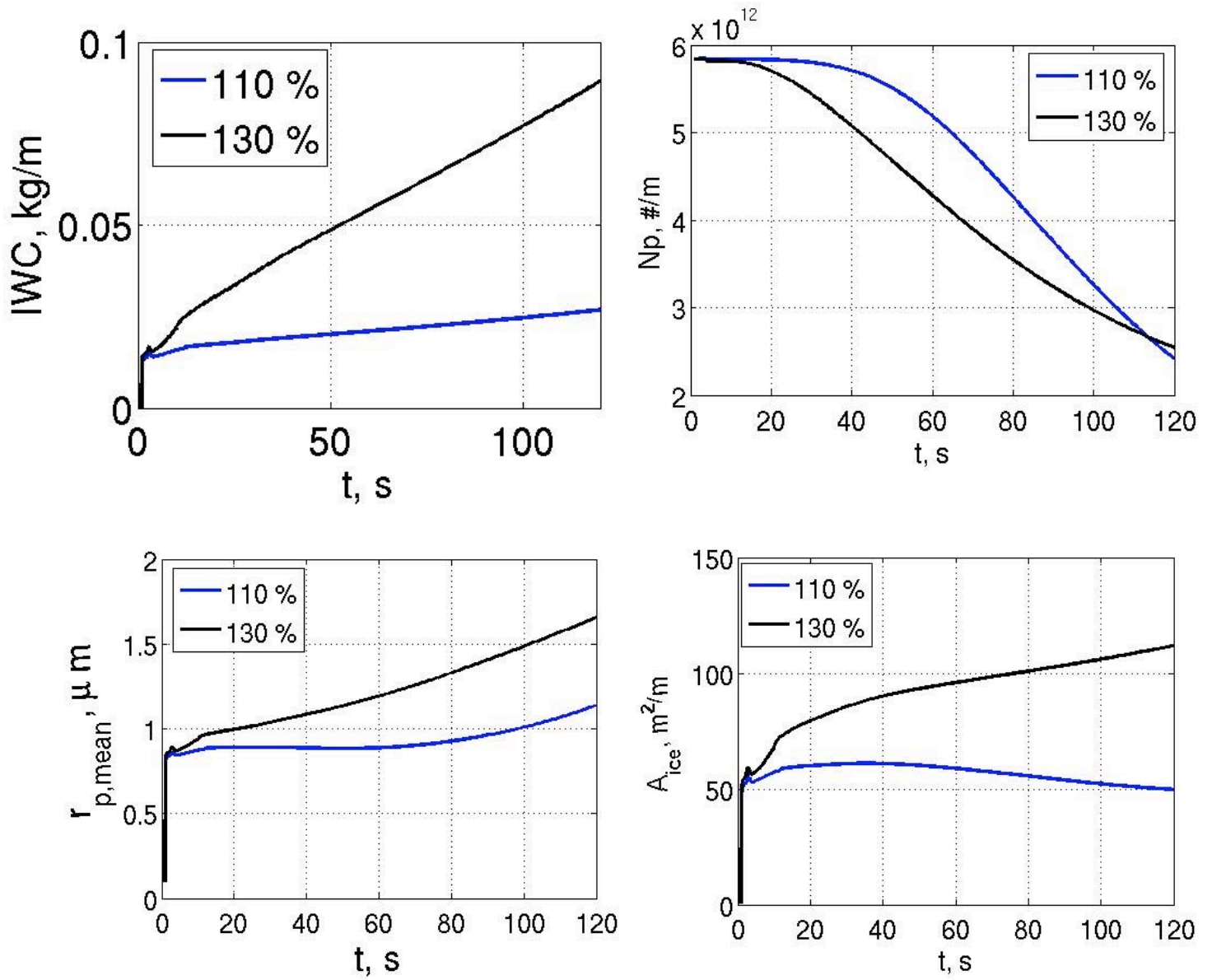


Fig. 12.30. Comparison of ice growth for $\text{RH}_i = 110\%$; and $\text{RH}_i = 130\%$;

5.6 Constant water vapor simulations

Case 1 was carried out with idealized Gaussian initial jets. The shape of these jets (Gaussian) differs from the shape of the jets in the Boeing initial data (used in cases 2 and 3), but the total water vapor content in the jets was matched between the two initial conditions. An interesting trend can be seen from the plots, that although the average ice particle size is increasing, the total IWC decreases at late times. This is attributed again to the depletion effect (see SL07)

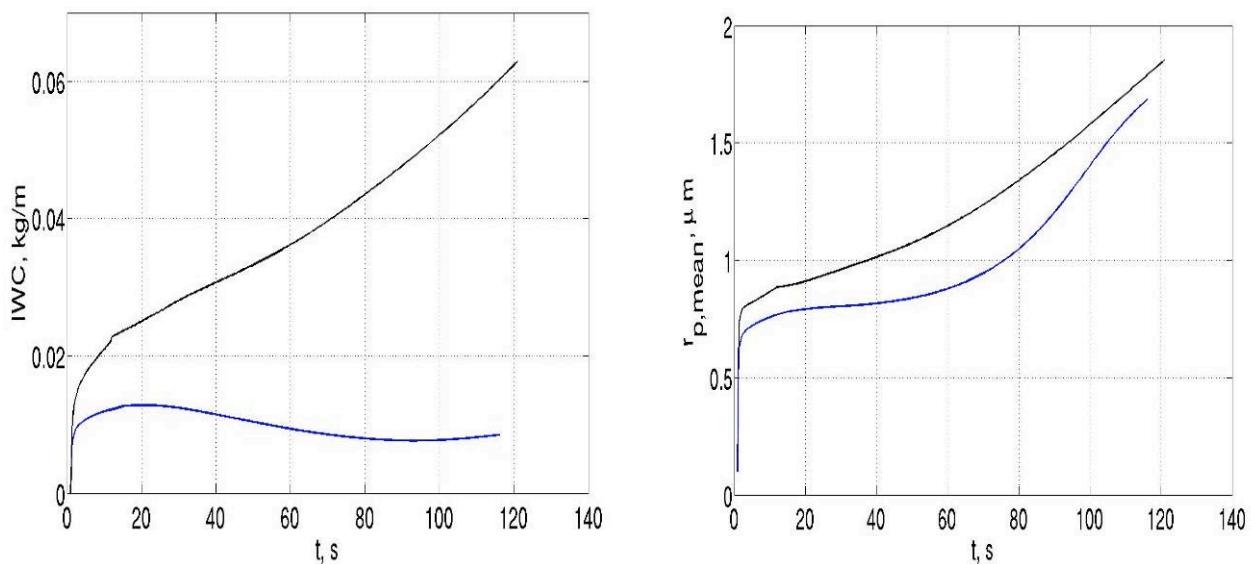


Figure 12.31: Ice water content and Mean ice particle radius for case 1. (Black – Const. RH at 110% Blue – Const. water vapor)

5.7 Comparison of 2 minute simulations with Boeing-WVU and SL07

The ice properties predicted by the 2 minute simulations show some significant differences from the results from Boeing, and in the first 20 seconds, and with the results from the contrail intercomparison case in Figs. 12.12, 12.13, 12.14. This latter 20 second case will henceforth be referred to as STAN-short. At the time this report was prepared we do not have report quality figures to illustrate these differences. Figure 12.32 is included as preliminary plots to give the reader a sense of the differences.

We are currently investigating this mismatch. Possible causes for this are:

1. Turbulence seeding into the jet is not necessarily the same for the current 2 minute calculations (henceforth referred to as STAN-long) and STAN-short, because the former uses 10 times bigger domain in the flight direction to capture Crow instability, when present. This

difference in domain sizes causes difference in the energy content of the turbulence seed, possibly having an impact on the ice properties.

2. Possibility of some inconsistency in the initialization of ice particles for the STAN-long case is being examined.

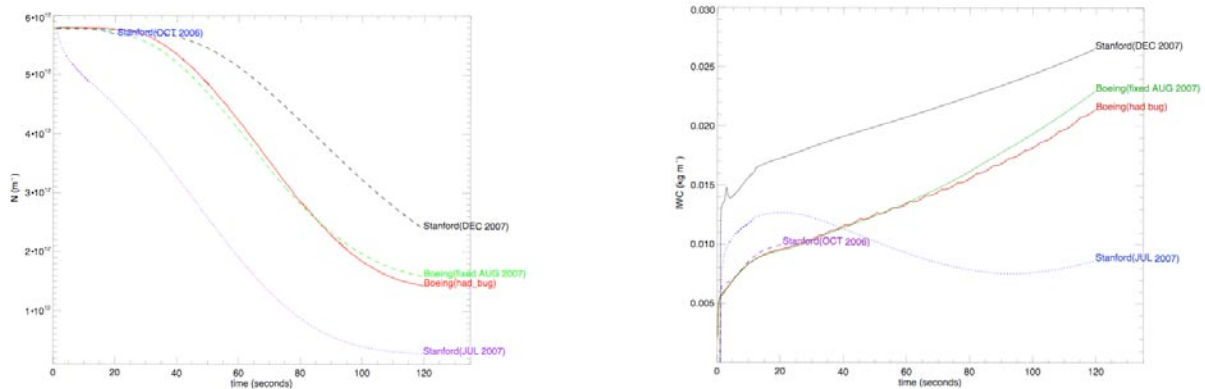


Figure 12.32: Comparison of ice nuclei number per meter (left) and total ice water content (right) between the Stanford and Boeing calculations over 2 min. horizon. The case marked Stanford (July 2007) is a calculation using Gaussian initial conditions for the wake vortex. Stanford (Dec 2007) is the calculation with the B767 (Boeing) initial conditions. Stanford (Oct 2006) is the data from the short domain (20 sec. horizon) calculation.

We have launched a diagnostic test simulation where the STAN-short domain (which is one wing span long in the flight direction) is stacked 10 times to match the STAN-long domain size (10 wing spans). This will make the geometric parameters between the two cases match each other, allowing a direct probe into the cause of difference. After this investigation the STAN-long results can be compared to Boeing-WVU 2 minute simulations.

Sorting out these issues will require additional time. We hope to understand the reasons for the differences during the first phase of a new study under FAA's support. In this study the LES capability will be extended to allow simulations up to 10-20 minute time horizon with effects of atmospheric turbulence and wind shear included.

Summary

1. The computational tools for conducting large-eddy simulations of aircraft contrails were developed. These tools combine high-order spectral-like finite difference discretization of the Eulerian flow field with a simple Lagrangian microphysical model of the contrail ice-microphysics.
2. The computational model was tested on a variety of fluid dynamic test cases and the micro-physical model was tested against a suite of simple test cases designed by Boeing.

Detailed tests were also conducted to assess grid convergence of the flow fields and the convergence of the hybrid Eulerian-Lagrangian ice-microphysical model.

3. The Stanford LES model was compared with the Boeing-WVU LES model for passive tracer representative of engine exhaust, and contrail comparison between the two simulations over the first 20 sec. showed that flow fields simulated by these two codes were quite similar. Although the details of ice particle distributions predicted by these codes showed some significant differences, gross properties of the contrail ice such as contrail ice mass, ice mass density, etc. were rather similar.
4. A detailed study of early-stage (up to 20 seconds) contrails was performed using high-fidelity large eddy simulations to characterize trends in contrail growth for different atmospheric temperature, relative humidity, ice nuclei number density and initial ice particle size. Ambient temperature and relative humidity were found to be the most critical variables among the above.
5. A small selected set of cases were run out to 2 minutes of contrail evolution to assess the impact of the atmospheric variables of the predicted contrail properties over this intermediate time of evolution. As in the early stage evolution the ambient relative humidity (degree of supersaturation with respect to ice, RH_i) affected the contrail properties in a significant manner. The vertical distribution of the ambient relative humidity also affected the overall contrail ice properties. Contrails in an ambient atmosphere of higher RH_i contained higher ice mass, higher average ice particle radius and ice particle surface area.
6. Over the 2 minute time horizon the contrail formed two distinct regions of significant ice growth and accumulation. a) In the region near the descending vortex pair the average ice particle size grew to about 1 micron with an abundance of smaller ice particles. The vertical motion causing elongation of the contrail. b) The wake of the vortex pair stretching back to the flight altitude contained larger ice particles, although fewer in number density, contributed dominantly to the total ice mass. These ice particles detrained from the 'head' or the 'Rankine oval' associated with the vortex wake, and continued to grow in the wake. The simulations did not seed any atmospheric turbulence, and there was no significant indication of the Crow instability over the 2 minute time horizon. Based on previous studies of Crow instability it is expected that when atmospheric turbulence is present, the evolution of the wake is likely to be modified by this instability.
7. The capabilities of contrail LES calculations require significant further development to enable a study of the persistent contrails. Effects of atmospheric turbulence and wind shear, and effects of ice particle sedimentation need to be captured in simulations over a longer time horizon (say 20 minutes of evolution). Such calculations can then be used to inform the development and refinement of sub-grid scale contrail parametrizations for use with regional and global scale atmospheric models. Such an effort is underway with Prof. Mark Jacobson as the lead PI.

Journal and Report Publications

1. A.A. Shirgaonkar and S.K. Lele, "Interaction of Vortex Wakes and Buoyant Jets: A Study of 2-D Dynamics," *Physics of Fluids*, 2007.
2. A. A. Shirgaonkar and S. K. Lele, "Large eddy simulation of early stage aircraft contrails," TF Report -100, Department of Mechanical Engineering, Flow Physics and Computational Engineering Group, Stanford University, 2007 (referred as **SL07**).
3. A. A. Shirgaonkar, "Large eddy simulation of early stage aircraft contrails," Ph.D. Thesis, Department of Mechanical Engineering, Stanford University, December 2006.
4. A. A. Shirgaonkar and S. K. Lele, "On the extension of the Boussinesq approximation for inertia dominated flows," *Physics of Fluids*, 18, pp. 066601, 2006.

Conference Publications/Presentations

- A. A. Shirgaonkar and S. K. Lele, "Inertia and compressibility effects in the Boussinesq approximation," Abstract GG.00003, APS Division of Fluid Dynamics 59th Annual Meeting, Tampa, Florida, 2006.
- A. A. Shirgaonkar and S. K. Lele, "Large Eddy Simulation of Contrails: Effect of Atmospheric Properties," AIAA Paper 2006 -1414, 44th AIAA Aerospace Sciences Meeting and Exhibit, Reno, NV, January 2006.
- A. A. Shirgaonkar and S. K. Lele, "Large eddy simulation of ice particle growth in aircraft contrails," Abstract BN.00004, presented at the APS Division of Fluid Dynamics 58th Annual Meeting, Chicago, IL, Nov. 2005.
- A. A. Shirgaonkar and S. K. Lele, "High-resolution Simulations of Aircraft Wake-Exhaust Mixing With Applications to Contrail Formation," AIAA Paper 2005-4909, 35th AIAA Fluid Dynamics Conference and Exhibit, Toronto, Canada, June 2005.

Plans for further study (beyond this project)

Simulations of contrails over longer times up to 20-30 minutes are needed to better understand the atmospheric impact of persistent contrails and the processes leading to contrail-induced cirrus clouds. These simulations will need to take into account the effects associated with atmospheric turbulence and wind shear. The microphysical model used in the simulation may also need to be extended to better model the dynamical processes in an aging contrail, such as the precipitation of large ice particles. More realistic ambient RH_i profiles can be used, in addition to the constant water vapor and constant RH_i profiles.

References

Anderson, B. E., Winstead, E., Hudgins, C., Plant, J., Branhan, H.-S., Thornhill, L., Boudries, H., Canagaratna, M., Miake-Lye, R., Workhoudt, J., Worsnop, D., Miller, T., Ballenthin, J., Hunton, D., Viggiano, A., Pui, D., Han, H.-S., Blake, D. and McEchern, M. "Overview of results from the NASA Experiment to Characterize Aircraft Volatile Aerosol and Trace Species Emissions (EXCAVATE)," Proceedings of the AAC-Conference, June 30-July 3, Friedrichshafen, Germany, 2003.

Appleman, H. "The formation of exhaust condensation trails by jet aircraft," Bull. American Meteorol. Soc., 34, 1420, 1953.

Brown, R. C., Miake-Lye, R. C., Anderson, M. R. and Kolb, C. E. "Aerosol dynamics in near-field aircraft plumes," J. Geophys. Res., 101 (D17), 22,939-22,953, 1996.

Chlond, A. "Large eddy simulation of contrails," J. Atmos. Sci., 55 (5), 196-719, 1998.

Durbeck, T. and Gerz, T. "Large-eddy simulation of aircraft exhaust plumes in the free atmosphere: effective diffusivities and cross-sections," Geophys. Res. Lett., 22 (23), 3203-3206, 1995.

Fahey, D. W. "In-situ observations in aircraft exhaust plumes in the lower stratosphere at midlatitudes," J. Geophys. Res., 100 (D2), 30653074, 1995.

Gierens, K. M. "Numerical simulations of persistent contrails," J. Atmos. Sci., 53 (22), 3333-3348, 1996.

Jacobson, M. Z. and Seinfeld, J. H. "Evolution of nanoparticle size and mixing state near the point of emission," Atmos. Environ., 38, 1839-1850, 2004.

Karcher, B. "Transport of exhaust products in the near trail of a jet engine under atmospheric conditions," J. Geophys. Res., 103 (D14), 17,129-17,148, 1994.

Karcher, B., Hirschberg, M. M., and Fabian, P. "Small scale chemical evolution of aircraft exhaust species at cruise altitudes," J. Geophys. Res., 101 (D10), 15,169-15,190, 1996.

Klima, K. and Waitz, I. "Assessment of a global contrail modeling method," Proceedings of the TAC-Conference, June 26-29, Oxford, UK, 2006.

Kraabol, A. G., Flatoy, F. and Stordl, F. "Impact of NO_x emissions from subsonic aircraft: Inclusion of plume processes in a three-dimensional model covering Europe, North America, and the North Atlantic," J. Geophys. Res., 105, 3573-3581, 2000.

Lee, D., Clare, P., Haywood, J., Karcher, B., Lunnin, R., Pilling, I., Slingo, A. and Tilston, J. "Identifying the uncertainties in radiative forcing of climate from aviation-related cirrus," DERA/AS/PTD/CR000103, UK Ministry of Defense, 2000.

Lewellen, D. C. and Lewellen, W. S. "The effects of aircraft wake dynamics on contrail development," J. Atmos. Sci., 58, 390-406, 2001.

Lukachko, S. P. and Waitz, I. A. "Engine design and operational impacts on particulate matter precursor emissions," ASME Turbo Expo 2005, Reno-Tahoe, Nevada, GT2005, 2005.

Marquart, S. and Mayer, B. "Towards a reliable GDM estimation of contrail radiative forcing," Geophys. Res. Lett., 29 (8), 1179, 2002.

- Meilinger, S. K., Karcher, B. and Peter, T. "Microphysics and heterogeneous chemistry in aircraft plumes - high sensitivity on local meteorology and atmospheric conditions," *Atmospheric Chemistry and Physics*, 5, 533-545, 2005.
- Miake-Lye, R. C. "Advancing the understanding of aviation's global impact," PARTNER Report No. PARTNER-COE-2005-003, November 2005.
- Paoli, R., Helie, J. and Poinso, T. "Contrail formation in aircraft wakes," *J. Fluid Mech.*, 502, 361-373, 2004.
- Ponater, M., Marquart, S. and Sausen, R. "Contrails in a comprehensive global climate model: Parameterization and radiative forcing results," *J. Geophys. Res.*, 107 (D13), 4164, 2002.
- Penner, J., Lister, D., Griggs, D., Dokken, D. and McFarland, M., eds. "Aviation and the global atmosphere," Intergovernmental Panel on Climate Change, Cambridge Univ. Press, 1999.
- Quackenbush, T. R., Teske, M. E. and Bilanin, A. J. "Dynamics of exhaust plume entrainment in aircraft wake vortices," AIAA Paper 96-0747, 1996.
- Sausen, R., Isaksen, I., Grewe, V., Hauglustaine, D., Lee, D., Myhre, G., Kohler, M., Pitari, G., Schumann, U., Stordal, F. and Zerefos, C. "Aviation radiative forcing in 2000: An update on IPCC (1999)," *Meteorologische Zeitschrift*, 14(4), 555-561, 2005.
- Schrader, M. L. "Calculations of aircraft contrail formation critical temperatures," *J. Applied Meteorol.*, 36(12), 1725-1729, 1997.
- Schumann, U., Konopka, P., Baumann, R., Busen, R., Gerz, T., Schlager, H., Schulte, P. and Volkert, H. "Estimate of diffusion parameters of aircraft exhaust plumes near the tropopause from nitric oxide and turbulence measurements," *J. Geophys. Res.*, 100 (D7), 14,147-14,162, 1995.
- Schumann, U. "On conditions for contrail formation from aircraft exhausts," *Meteorol. Zeitsch.*, 5, 423, 1996.
- Schumann, U. "Formation, properties and climatic effects of contrails," *Comptes Rendus Physique*, 6, 549-565, 2005.
- Sussman, R. and Gierens, K. M. "Lidar and numerical studies on the different evolution of vortex pair and secondary wake in young contrails," *J. Geophys. Res.*, 104 (D12), 2131-2142, 1999.
- Sussman, R. and Gierens, K. M. "Differences in early contrail evolution of two-engine versus four engine aircraft: Lidar measurements and numerical simulations," *J. Geophys. Res.*, 106 (D5), 4899-4911, 2001.
- Wuebbles, et al. "Workshop on the Impacts of Aviation on Climate Change: A report on findings and recommendations," PARTNER Report No. PARTNER-COE-2006-04, June 7-9, 2006, Cambridge, MA.

Detailed One-Dimensional Microphysical Modeling on Contrail Formation from Near-Field Aircraft Emission at Cruise

Aerodyne Research, Inc.

Background

The aviation industry has grown rapidly into an integral part of global economy and is expected to continue to expand (Wuebbles et al., 2006). Environmental concerns over aviation, especially the effects of aircraft emissions on the current and projected climate change, have also increased. Contrails and contrail-cirrus formed from aircraft emissions were identified by the International Panel on Climate Change (IPCC) as the most uncertain components of the aviation impacts on climate (Penner et al., 1999). Although many studies have been performed to understand formation mechanisms of contrails or contrail-cirrus, knowledge of contrails and contrail-cirrus chemistry and microphysics is still limited. To evaluate the effects of aviation contrails or contrail-cirrus on global climate change, it is essential to have an improved understanding of the critical parameters controlling chemical and microphysical processes during contrail and contrail-cirrus evolution.

Objectives

The objective of Aerodyne's work for Project 12 is to use and extend our one-dimensional microphysical modeling tool to study the evolution of contrails from aircraft emissions. Our microphysical model includes nucleation of new particles, condensational growth of condensable gases on existing particles, and coagulation of volatile aerosols. We seek to understand the impacts of atmospheric conditions (such as temperature, pressure, and relative humidity) and engine operation parameters (such as initial soot particle size and concentration) on ice particle formation and growth. We also utilize our modeling capability to study the effects of plume dilution history on the evolution of ice particles.

Technical Approaches

1. One-Dimensional Detailed Microphysical Model

In the Aerodyne microphysical model, the evolution of any gaseous or particulate species with respect to time (t) is described as (Kärcher, 1998; Wong et al., 2007):

$$\frac{dX_i}{dt} = \left. \frac{dX_i}{dt} \right|_{chemistry} + \left. \frac{dX_i}{dt} \right|_{mixing} + \left. \frac{dX_i}{dt} \right|_{microphysics} \quad (1)$$

where X_i is the mass fraction of gaseous species or the concentration of aerosol particles. The three terms on the right hand side (RHS) of Equation (1) correspond to the rates of production or disappearance from chemical reactions, wake dilution and mixing, and microphysical processes, respectively.

To evaluate the contribution of chemical reactions, the first term on the RHS of Equation (1) is expressed as:

$$\left. \frac{dX_i}{dt} \right|_{chemistry} = \dot{\omega}_i \cdot M_{w,i} \cdot \frac{1}{\rho_{pl}} \quad (2)$$

where $\dot{\omega}_i$ is the molar production rate of species i evaluated by CHEMKIN libraries (Lee et al., 1996), $M_{w,i}$ is the molecular weight of species i , and ρ_{pl} is the density of the plume. Note that Equation (2) applies to the gaseous species only, since particulate species do not participate in any of the chemical reactions in our model.

The contribution of wake dilution and mixing in Equation (1) is written as:

$$\left. \frac{dX_i}{dt} \right|_{\text{mixing}} = (X_i - X_{\text{amb},i}) \cdot \frac{df(t)}{dt} \cdot \frac{1}{f(t)} \quad (3)$$

where $f(t)$ is the exhaust gas mass fraction as a function of time t , which was estimated from the semi-empirical approach developed by Davidson and Wang (2002) or the empirical approach developed by Schumann et al. (1998). $X_{\text{amb},i}$ is the mass fraction of species i in the ambient.

The contribution of the microphysical processes in Equation (1) is described as the combination of three elements as:

$$\left. \frac{dX_i}{dt} \right|_{\text{microphysics}} = \left. \frac{dX_i}{dt} \right|_{\text{nucleation}} + \left. \frac{dX_i}{dt} \right|_{\text{coagulation}} + \left. \frac{dX_i}{dt} \right|_{\text{soot}} \quad (4)$$

where the first term on the RHS of Equation (4) describes the binary homogeneous nucleation of sulfuric acid (H_2SO_4) and water (H_2O). The newly developed kinetic quasi-unary nucleation theory (Yu, 2005, 2007) is incorporated into our model instead of classical nucleation theory to evaluate the nucleation rates of the volatile embryos. The formation rates of the embryos due to homogeneous binary nucleation are explicitly considered from the condensation and evaporation:

$$\frac{dn_i}{dt} = \beta_{i-1}n_{i-1} - \gamma_i n_i - \beta_i n_i + \gamma_{i+1} n_{i+1} \quad (i>2) \quad (5-1)$$

$$\frac{dn_2}{dt} = \frac{1}{2} \beta_1 n_1 - \gamma_2 n_2 - \beta_2 n_2 + \gamma_3 n_3 \quad (i=2) \quad (5-2)$$

$$\frac{dn_1}{dt} = 2\gamma_2 n_2 + \sum_{i=3}^m \gamma_i n_i - \sum_{i=1}^{m-1} \beta_i n_i \quad (i=1) \quad (5-3)$$

where the subscript i denotes the size of the embryos (containing i monomer units), n_i is the concentration of the embryos (i.e., X_i for the embryos), β_i is the condensation rate, γ_i is the evaporation rate of the embryo with size i , and m is the largest embryo tracked in the model. Note that in this theory, we assume that water reaches equilibrium with embryos of different sizes immediately such that the binary nucleation can be treated as unary nucleation of sulfuric acid.

The second term on the RHS of Equation (4) corresponds to the coagulation of different volatile particles and the condensational growth of sulfuric acid on volatile embryos or droplets (Seinfeld and Pandis, 1998):

$$\frac{dn_k}{dt} = \frac{1}{2} \sum_{i+j=k} K_{ij} n_i n_j - \sum_{i=1}^l K_{ik} n_i n_k \quad (6)$$

where i, j, k and l denote the size of the volatile particles. These indices do not go beyond the biggest embryo tracked in Equation (5-1), which is a user-specified value set at 40. Otherwise, we use fully stationary sectional bin approach (Jacobson and Turco, 1995) to track larger particles. In this case, l denotes the number of sectional bin tracked, and n_i and n_j are the concentrations of the particle droplets in the i -th and j -th bins. Note that mass conservation has to be taken into account across the boundary between the embryos and the binned particles. K_{ij} is the Brownian coagulation kernel between two particles with diameter d_i and d_j (Fuchs, 1989):

$$K_{ij}(d_i, d_j) = \frac{8\pi \bar{d} \bar{D}}{\bar{d}/(\bar{d} + \bar{\delta}) + 4\bar{D}/(\bar{d} + \bar{c})} \quad (7)$$

where $\bar{d} = (d_i + d_j)/2$ is the average diameter, $\bar{D} = (D_i + D_j)/2$ is the average diffusivity, $\bar{c} = (c_i^2 + c_j^2)^{1/2}$ is the mean square particle speed, and $\bar{\delta} = (\delta_i^2 + \delta_j^2)^{1/2}$ is the mean free distance between the particles.

Note that in Equation (6), the first term on the RHS corresponds to the formation of the particle with size k , and the second term describes the disappearance of the particle with size k . Since quasi-unary nucleation theory explicitly considers sulfuric acid condensing on or evaporating from embryos, as shown in Equations (5-1)–(5-3), the condensational growth considered in Equation (6) only takes the interactions between sulfuric acid monomer and larger particles that are not included in the nucleation process into account. This step is treated similarly to what is done in nucleation, but the condensational rates are estimated based on the coagulation rates mentioned above. The amount of water change from this process is also calculated based on the equilibrium compositions of different particle sizes.

The third term on the RHS of Equation (4) describes the microphysical interactions between the volatile species and the soot particles. The size evolution of the soot particles is expressed as the combination of soot activation and condensational growth:

$$\frac{dm_i}{dt} = \left. \frac{dm_i}{dt} \right|_{activation} + \left. \frac{dm_i}{dt} \right|_{condensation} \quad (8)$$

where m_i is the time-dependent condensed mass on soot particles in the i -th size bin. The soot activation is further divided into adsorption and the scavenging:

$$\left. \frac{dm_i}{dt} \right|_{activation} = \left. \frac{dm_i}{dt} \right|_{adsorp.} + \left. \frac{dm_i}{dt} \right|_{scav.} \quad (9)$$

where adsorption is expressed as:

$$\left. \frac{dm_i}{dt} \right|_{adsorp.} = \frac{1}{4} \cdot \alpha_d \cdot \bar{c} \cdot d_{p,i}^2 \cdot (1 - \theta_i) \cdot (C_s M_{w,s} + C_a M_{w,a}) \quad (10)$$

in which α_d is the mass accommodation number set at 0.018, \bar{c} is the mean thermal speed of SO_3 and H_2SO_4 , θ_i is the surface coverage of the soot particles in size bin i , C_s and C_a and $M_{w,s}$ and $M_{w,a}$ are the concentrations and the molecular weights of SO_3 and H_2SO_4 molecules, respectively.

The scavenging of volatile H_2SO_4 - H_2O embryos and droplets can be written as:

$$\left. \frac{dm_i}{dt} \right|_{\text{scav}} = \frac{1}{4} \cdot \pi \cdot \sum_j B_{i,j} N_j \left[\frac{d_j}{d_{p,i}} \right]^2 (1 - \theta_i) \cdot M_{w,j} \quad (11)$$

where $B_{i,j}$ is the coagulation kernel between soot in size bin i and volatile droplets in size bin j , $d_{p,i}$ is the diameter of soot in size bin i , N_j is the number density of the volatile droplets, d_j is the diameter of the volatile droplets, and $M_{w,j}$ is the molecular weight of the volatile droplets in size bin j .

Finally, the condensational growth of soot particles is described as contributions from both sulfuric acid and water:

$$\left. \frac{dm_i}{dt} \right|_{\text{condensation}} = \left. \frac{dm_i}{dt} \right|_{\text{sulfur}} + \left. \frac{dm_i}{dt} \right|_{\text{water}} \quad (12)$$

in which:

$$\left. \frac{dm_i}{dt} \right|_{\text{sulfur}} = 2\pi G_i N_0 \sum_j \left[D_j d_{p,i} \theta_i \left(\frac{P_{a,j} - \kappa P_{a,j}^\infty}{RT} \right) \cdot M_{w,j} \right] \quad (13)$$

and

$$\left. \frac{dm_i}{dt} \right|_{\text{water}} = 2\pi G_i N_0 D_v d_{p,i} \theta_i \left(\frac{P_v - \kappa P_v^\infty}{RT} \right) \cdot M_{w,v} \quad (14)$$

where D_j and D_v are the diffusivities of sulfuric acid and water vapors, G_i is the collision factors, $P_{a,j}$ and $P_{a,j}^\infty$ are partial pressure and saturation vapor pressure of volatile particle j , and P_v and P_v^∞ are vapor pressure and saturation vapor pressure of water.

2. Algorithms for Constructing Plume Dilution Profiles

The semi-empirical, self-similar approach developed by Davidson and Wang (2002) was used to determine plume dilution history, i.e., the exhaust gas mass fraction evolution as a function of time ($f(t)$ in Equation (3)). In the Davidson and Wang algorithm, the centerline velocity of a two-stream coflowing jet in the weakly advected, strong jet region can be expressed as:

$$\frac{u_{CL}(x) - u_a}{u_a} = \frac{1}{\sqrt{I_m k}} \frac{\sqrt{M_{e0}}}{u_a \cdot x} \quad (15)$$

where x is the axial distance downstream, $u_{CL}(x)$ is the centerline velocity as a function of x , u_a is the coflowing velocity (cruising speed in this case), M_{e0} is the initial excess momentum per unit density calculated from the velocities at the engine exit plane, I_m is an integral constant with a value of 1.74, and k is the spread constant with a value of 0.107.

The centerline exhaust gas mass fraction in the same region can be described as:

$$f_{CL}(x) = \frac{\sqrt{I_m}}{I_{qc} \cdot k} \frac{\sqrt{M_{e0}}}{(u_0 - u_a) \cdot x} \quad (16)$$

where $f(x)$ is the exhaust gas mass fraction as a function of x , I_{qc} is an integral constant with a value of 1.99, and u_0 is the initial jet velocity, which is the mass flow rate weighted average velocity of the core and the bypass flows.

In the strongly advected, weak jet region, the centerline velocity and concentration profiles are expressed as:

$$\frac{u_{CL}(x) - u_a}{u_a} = \left[\frac{C_{jk}^2}{9\pi k^2} \right]^{1/3} \left[\frac{\sqrt{M_{e0}}}{u_a \cdot x} \right]^{2/3} \quad (17)$$

$$f_{CL}(x) = \frac{1}{I_c} \left[\frac{C_{jk}\pi}{3k} \right]^{2/3} \left[\frac{\sqrt{M_{e0}}}{u_a \cdot x} \right]^{2/3} \left[\frac{u_a}{u_0 - u_a} \right] \quad (18)$$

in which I_c is an integral constant with a value of 4.45. In both regions, the temperature evolution as a function of downstream distance is related to the mass fraction dilution history described in Equations (16) and (18) as:

$$\frac{T_{CL}(x) - T_a}{T_0 - T_a} = \frac{\sqrt{I_m}}{I_{qc} \cdot k} \frac{\sqrt{M_{e0}}}{(u_0 - u_a) \cdot x} \quad (\text{weakly advected, strong jet region}) \quad (19)$$

$$\frac{T_{CL}(x) - T_a}{T_0 - T_a} = \frac{1}{I_c} \left[\frac{C_{jk}\pi}{3k} \right]^{2/3} \left[\frac{\sqrt{M_{e0}}}{u_a \cdot x} \right]^{2/3} \left[\frac{u_a}{u_0 - u_a} \right] \quad (\text{strongly advected, weak jet region}) \quad (20)$$

Once the centerline properties are calculated, the velocity, temperature, and exhaust gas fraction in radial direction is described as:

$$\frac{U(r, x) - U_a}{U_{CL}(x) - U_a} = \frac{T(r, x) - T_a}{T_{CL}(r, x) - T_a} = \frac{f(r, x)}{f_{CL}(x)} = \exp \left[- \left(\frac{r}{b(x)} \right)^2 \right] \quad (21)$$

where $b(x)$ is calculated as:

$$b(x) = C_L \cdot k \cdot x \quad (\text{weakly advected, strong jet region}) \quad (22)$$

$$b(x) = C_L \cdot \left[\frac{3k \cdot x}{C_{jk}\pi} \right]^{1/3} \left[\frac{\sqrt{M_{e0}}}{u_a} \right]^{2/3} \quad (\text{strongly advected, weak jet region}) \quad (23)$$

where C_L is a constant with a value of 1 for radial velocity profiles and 1.19 for radial temperature and exhaust mass fraction profiles.

Alternatively, the empirical fit of exhaust mass fraction by Schumann et al. (1998) can also be used to estimate plume dilution history:

$$f_{CL}(x) = \frac{m_e}{m_f} \cdot \frac{1}{7000 \cdot t^{0.8}} \quad (24)$$

where m_e is the exhaust mass flow rate (including the core flow and the bypass flow), and m_f is the fuel flow rate.

Results and Discussions

1. Construction of Particle Size Distribution Lookup Table

We have performed 1-D detailed microphysical simulations for PW4056 engines equipped on Boeing 767 with a wingspan of 47.5 m. The parameters used for these simulations are listed in Table 1.

Table 1. Parameters Used for 1-D Microphysical Simulations

Cruise Altitude	35,000 <i>ft</i>
Ambient Temperature, T_a	218.8 <i>K</i>
Ambient Pressure, P_a	23.835 <i>kPa</i>
Air Density, ρ_a	0.3795 <i>kg/m³</i>
Cruise Speed, u_a	236.789 <i>m/s</i> (0.8 <i>M</i>)
Net Thrust, Γ	42.18 <i>kN</i>
Core Mass Flow Rate, m_c	52.72 <i>kg/s</i>
Bypass Mass Flow Rate, m_b	247.033 <i>kg/s</i>
Fuel Mass Flow Rate, m_f	0.685 <i>kg/s</i>
Mass Flow Rate into the Engine, m_{in} ($=m_b + m_c - m_f$)	299.068 <i>kg/s</i>
Bypass Ratio ($=m_b / m_c$)	4.686
Core Total Temperature at Engine Exit, T_c	590.23 <i>K</i>
Bypass Total Temperature at Engine Exit, T_b	288.36 <i>K</i>
Core Flow Velocity at Engine Exit, u_c	444.60 <i>m/s</i>
Bypass Flow Velocity at Engine Exit, u_b	310.76 <i>m/s</i>

The resulting ice particle size distributions at 5 wingspans downstream were compiled into a lookup table under different relative humidity with respect to ice (RHi), ranging from 80% to 110%. For each level of relative humidity, the ice particle size distribution at each radial location was fitted into a log-normal distribution as:

$$N_i(D_p) = \frac{N_0}{\sqrt{2\pi \ln(\sigma)^2}} \exp\left[-\frac{(\ln(D_p) - \ln(\mu))^2}{2 \ln(\sigma)^2}\right] \quad (25)$$

where $N_i(D_p)$ is the number density of ice particles with a diameter of D_p , N_0 is an integration constant, σ is the standard deviation, and μ is the geometric mean diameter of the distribution. The parameters (N_0 , σ , and μ) needed to construct size distribution for ice particles at 5 wingspans downstream were tabulated in the lookup table. Selected data from the lookup library are listed in Table 2.

Table 2. Selected data in the lookup table for the ice particle size distributions at 5 wingspans downstream

		Centerline	70% Radial	30% Radial	5% Radial	2% Radial
RHi = 110%	N_o (cm^{-3})	4960.7029	2953.1607	1239.5701	142.4473	310.8565
	μ (nm)	1024.553	1026.039	1039.936	742.000	232.482
	σ	1.0246	1.0209	1.0204	1.0132	1.0743
RHi = 100%	N_o (cm^{-3})	4986.2831	2968.4246	1252.2107	150.6379	350.1825
	μ (nm)	1022.527	1023.169	1033.613	719.007	212.020
	σ	1.0247	1.0210	1.0206	1.0139	1.0841
RHi = 90%	N_o (cm^{-3})	5004.5123	2983.9632	1267.6280	158.8352	398.8061
	μ (nm)	1020.499	1020.279	1027.254	696.311	191.141
	σ	1.0248	1.0211	1.0209	1.0147	1.0965
RHi = 80%	N_o (cm^{-3})	5022.3777	2994.6400	1281.1992	168.8202	459.9446
	μ (nm)	1018.482	1017.400	1020.942	672.306	170.053
	σ	1.0249	1.0212	1.0211	1.0156	1.1126

The effects of plume radial location and ambient relative humidity on the number density (N_o) and geometric mean diameter (μ) of ice particles at 5 wingspans downstream listed in the lookup table can also be shown in Figure 1. In Figure 1a, N_o drops sharply with increasing radial direction, and μ increases slightly with increasing radial direction until around 5% momentum radius where particle size starts to drop significantly. Figure 1b demonstrates that ice particles are larger when levels of RHi are higher.

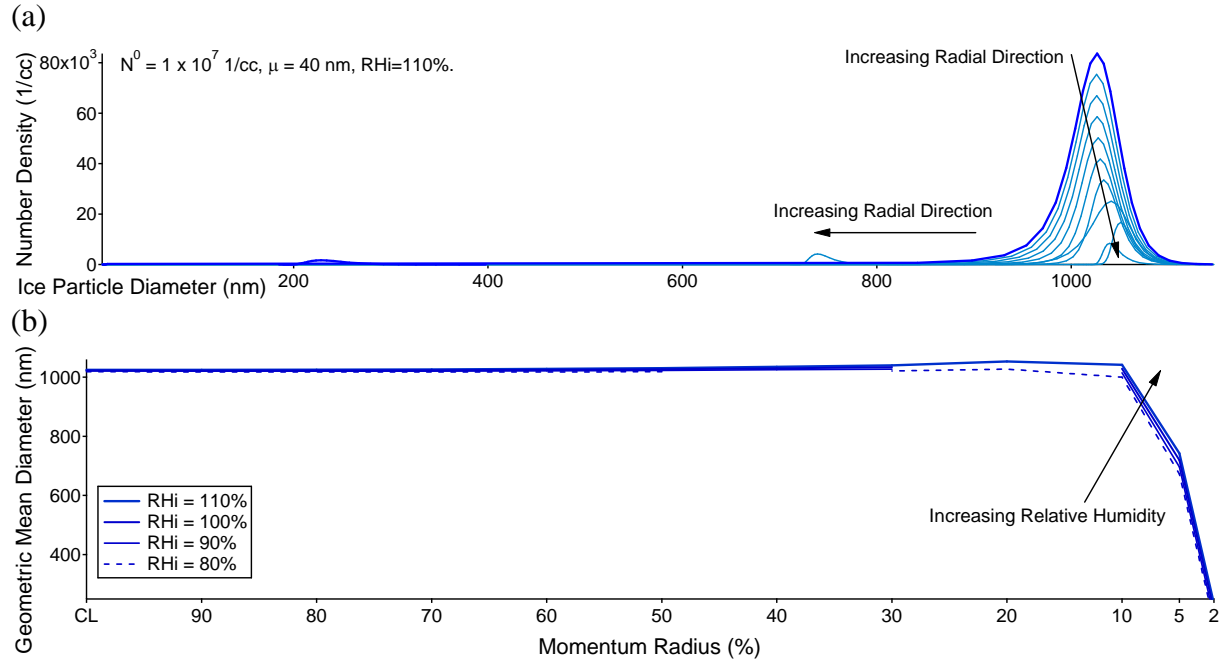


Figure 1. (a) Ice particle size distribution at different radial locations at 5 wingspans downstream; (b) Effects of ambient relative humidity with respect to ice on the geometric mean diameter of ice particles at 5 wingspans downstream.

2. Parametric Studies of Ambient Conditions and Initial Properties of Soot Particles

We have performed parametric analysis studying the sensitivity of the particle size distribution to ambient relative humidity with respect to ice (RHi), initial number density of soot particles, and

initial soot particle size. We studied the effects of four different levels of ambient RH_i (110%, 100%, 90%, 80%), three different initial number density (N^0) of soot particles ($1.0 \times 10^7 \text{ cm}^{-3}$, $5.0 \times 10^7 \text{ cm}^{-3}$, and $1.0 \times 10^8 \text{ cm}^{-3}$), and three different initial size distributions of soot particles (with geometric mean diameter of 20 nm, 40 nm and 80 nm, respectively). All the simulations were performed up to a distance of 30,000 m downstream.

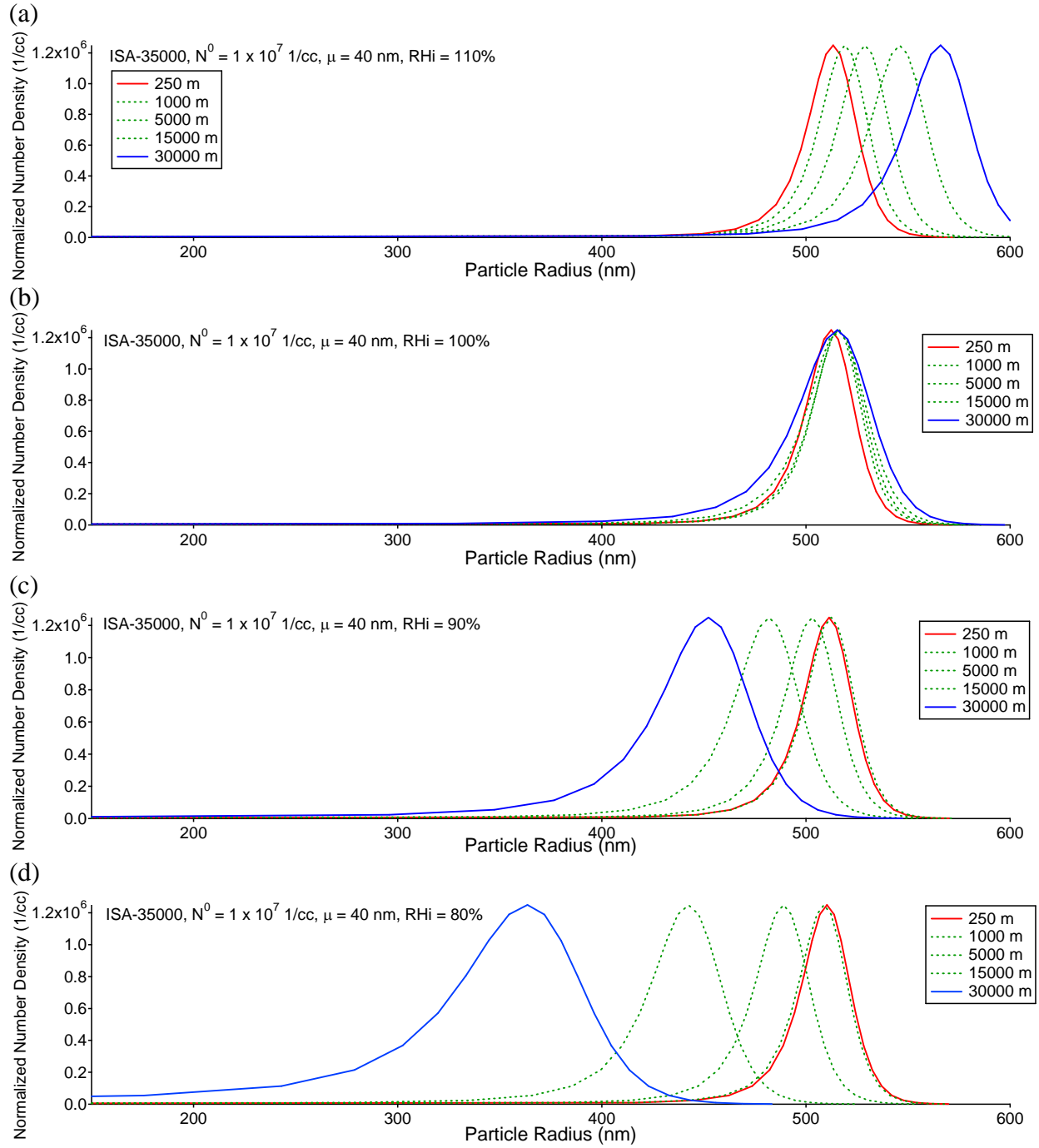


Figure 2. Ice particle size distribution at different downstream locations when N^0 is $1.0 \times 10^7 \text{ cm}^{-3}$ and μ is 40 nm under ambient RH_i of (a) 110%; (b) 100%; (c) 90%; (d) 80%.

Figure 2 shows the effects of ambient relative humidity and downstream distance on the evolution of ice particles. As shown in the figures, the mean radius of ice particles in the plume centerline reaches around 510 nm at about 5 wingspans downstream (~250 m) for all cases (RHi from 80% to 110%). For ambient RHi of 110% (Figure 2a), the ice particles continue to grow as downstream distance increases, and the mean radius of ice particles in the plume centerline reaches around 570 nm at 30,000 m downstream. For ambient RHi of 100% (Figure 2b), the ice particles do not grow significantly after 250 m downstream, and ice particle size stays about the same. For ambient RHi below 100% (Figures 2c and 2d), the ice particles evaporate as downstream distance increases. This is especially obvious when RHi is lower at 80% (Figure 2d), where the mean radius of ice particles is smallest (~350 nm) at 30,000 downstream among all cases.

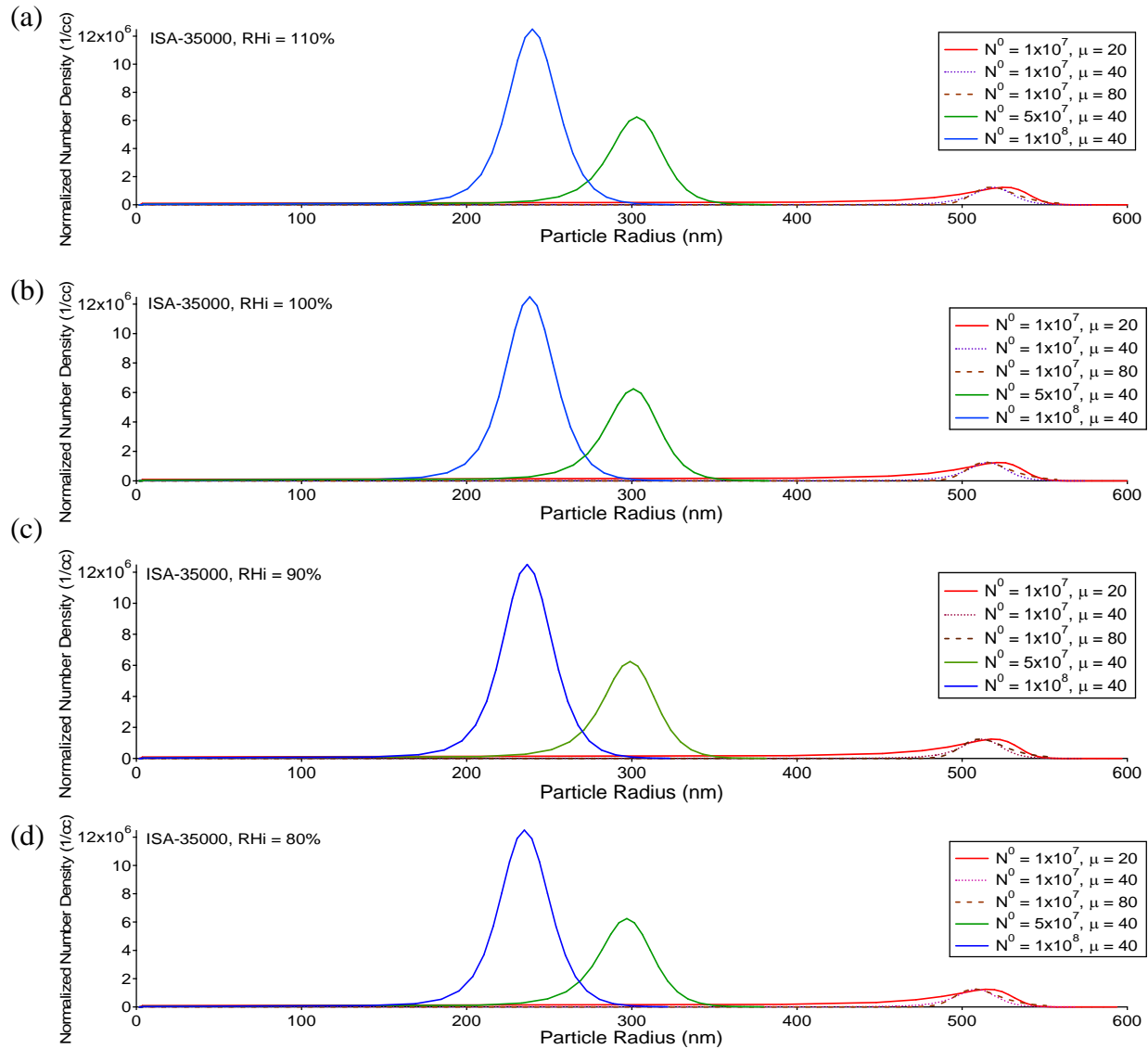


Figure 3. Effects of initial soot particle properties on ice particle size distribution at 1000 m downstream under ambient RHi of (a) 110%; (b) 100%; (c) 90%; (d) 80%.

Figure 3 shows the effects of initial properties of soot particles on ice particle size distribution in the plume centerline at 1000 m downstream. As shown in the figures, the ice particle size decreases with increasing initial number density of soot particles. This is because that more soot particle surface area is available for water vapor condensation when initial number density of soot particles is higher, and each particle has a smaller amount of water condensed on since total amount of water available is the same. We can also see from the figures that initial soot particle size does not seem to affect the particle size distribution at 1000 m downstream for $N^0 = 1 \times 10^7 \text{ cm}^{-3}$. This suggests that there is an equilibrium ice particle size under a given ambient condition and particle number density.

3. Studies of Dilution Histories and Trajectories

A simple trajectory study was firstly performed by comparing a smooth profile generated from Schumann algorithm and two fluctuating profiles from the Stanford Large Eddy Simulations (LES) after 5 wingspans downstream. In this study, the size of the monodisperse ice particles was not affected by the trajectories provided, as shown in Figure 4. However, it should be noted that the particles almost reached their equilibrium size before deviation of the profiles started at 5 wingspans downstream. The results suggest that the trajectories do not affect the size evolution of ice particles once they reach their final equilibrium state.

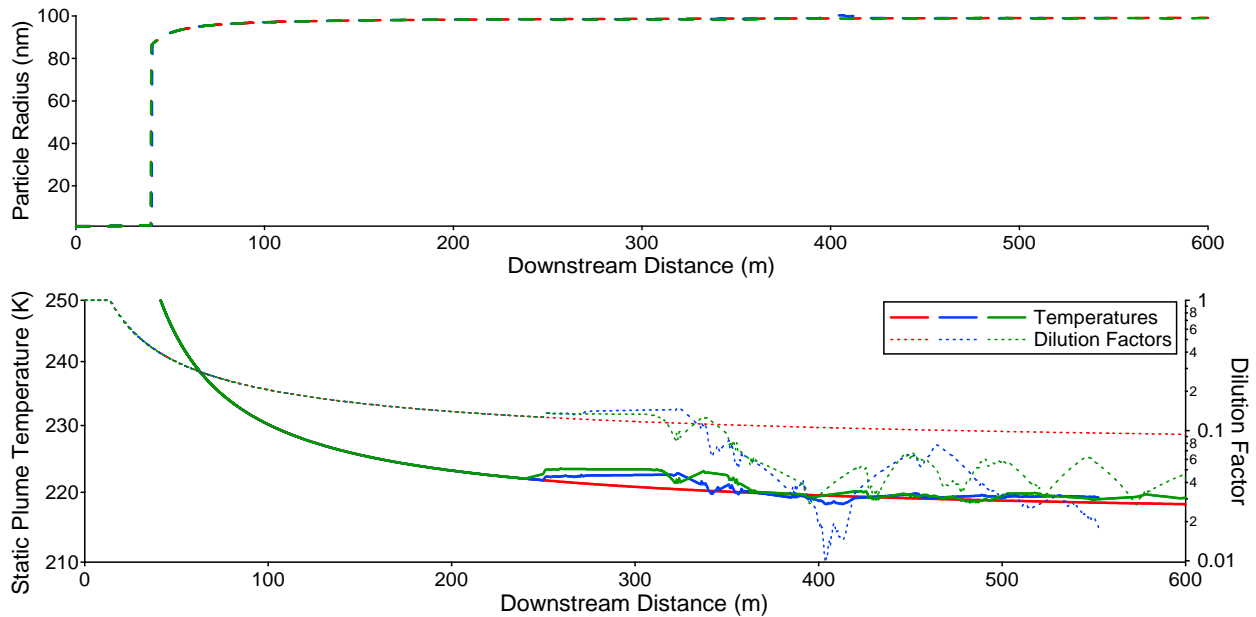


Figure 4. The size evolution of ice particles under three different dilution trajectories after 5 wingspans downstream.

To investigate the effects of dilution history on the evolution of ice particle size distribution before they reach equilibrium, the dilution histories under different RH_i were modeled using oscillating trajectories from the LES results by Garnier et al. (1997) for the first 65 m. After 65 m, smooth trajectories from the Schumann algorithm were used. The ice particle formation following the Davidson-Wang trajectories was also studied for comparison. As shown in Figure 5, the size evolution of ice particles shows dependency on temperature histories before 65 m. However, the size distributions of ice particles do not deviate from each other significantly at

1000 m downstream between the Schumann and the Garnier trajectories, where the same final ambient state is reached. The results suggest that the growth of ice particles at cruise reaches equilibrium rapidly and is insensitive to the kinetics of the formation processes.

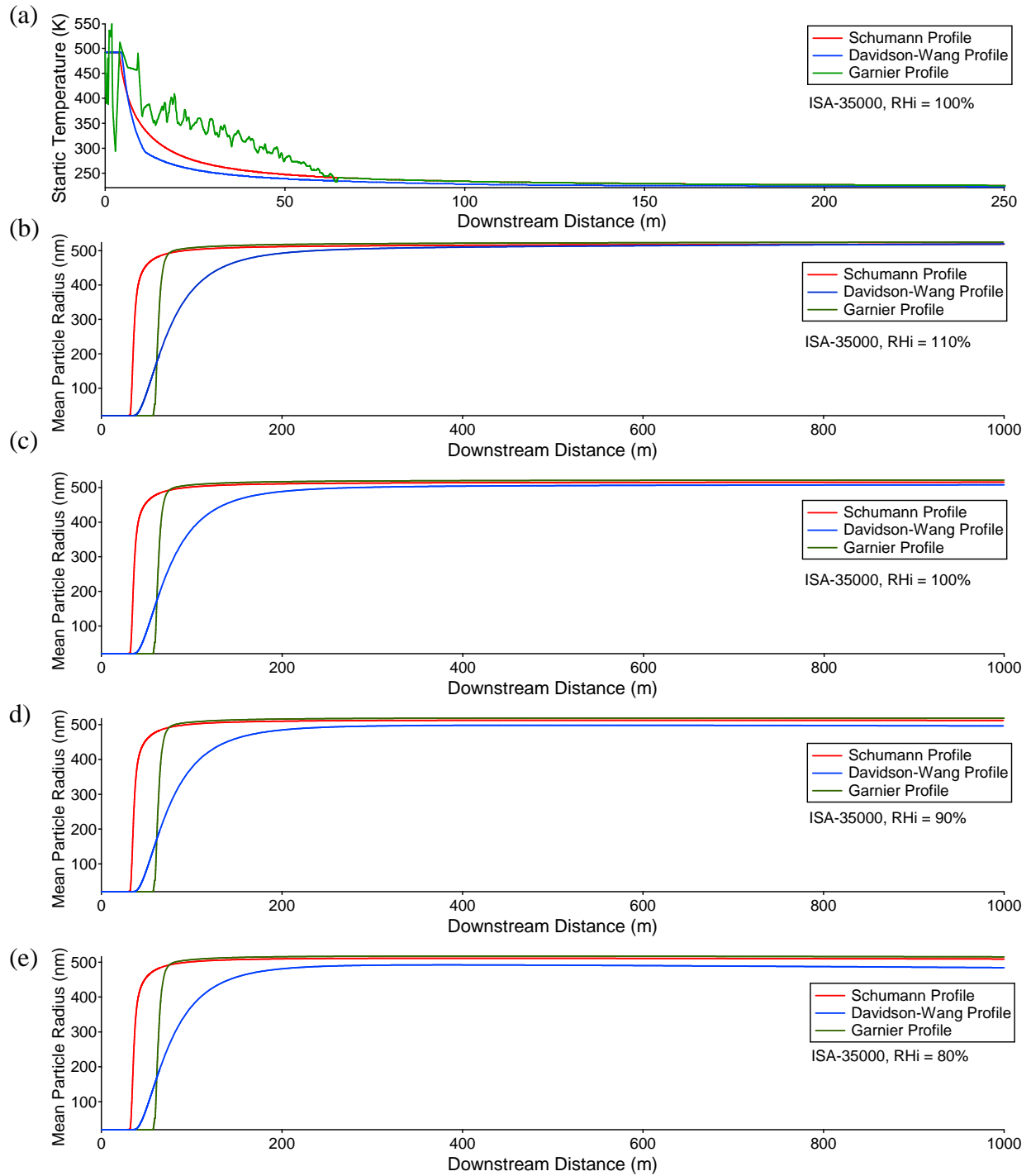


Figure 5. The size evolution of ice particles up to 1000 m downstream following (a) three different dilution trajectories before 65 m under RHi of (b) 110%; (c) 100%; (d) 90%; (e) 80%.

4. The effects of Ion-Assisted Nucleation

The effects of ion-assisted nucleation have been studied extensively in the literature. Although it is believed that ions are present in the aircraft emission at cruise and have great impacts on homogenous nucleation and formation on volatile sulfuric acid-water aerosols, their contribution to the formation of ice particles or early contrails is still uncertain. Here we investigated the effects of ion-assisted nucleation on the formation of ice particles using the same parameters listed in Table 1. The algorithms for ion-assisted nucleation are based on the model developed by Yu (2006). The initial ion concentration was assumed to be 1% of the initial sulfuric acid concentration. The ambient relative humidity was set at 110%. The initial soot particle number density was set at $1 \times 10^7 \text{ cm}^{-3}$, and initial geometric mean diameter of soot particles was set at 40 nm. The Schumann algorithm was used to calculate plume dilution history, and simulation was performed up to 1000 m downstream. As shown in Figure 6, the presence of ions does speedup the nucleation rates of homogeneous $\text{H}_2\text{SO}_4\text{-H}_2\text{O}$ particles, as evidenced by the significant enhancement of the embryo and droplet concentrations. However, the growth of ice coated soot particles was not affected, as shown in Figure 7, where only a slight increase of the ice particle size was predicted in the calculations.

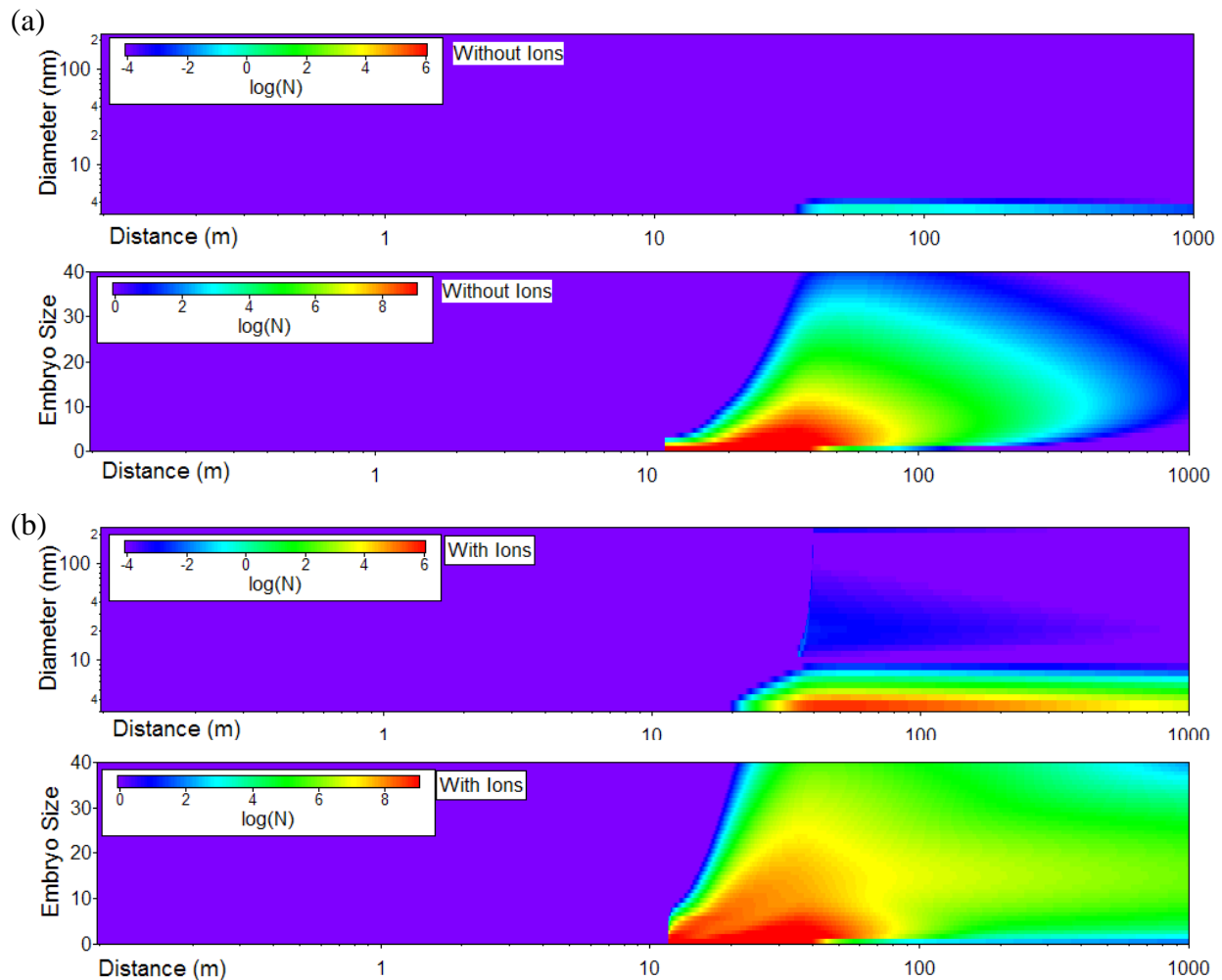


Figure 6. The predicted concentrations of $\text{H}_2\text{SO}_4\text{-H}_2\text{O}$ embryos and droplets when ion-assisted nucleation was (a) not included; (b) included.

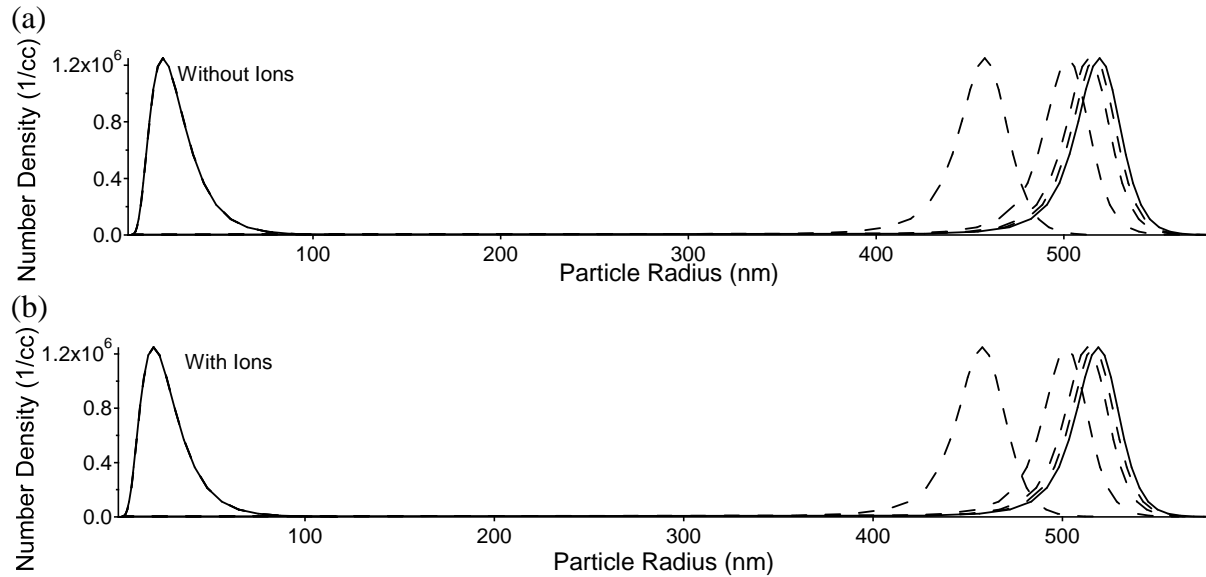


Figure 7. The predicted ice particle size up to 1000 m downstream when ion-assisted nucleation was (a) not included; (b) included.

5. Results for ISA-24000 Conditions

We have also performed 1-D microphysical simulation to calculate the ice particle size distributions for PW4056 engines under a different condition corresponding to 24,000 ft ISA. The ambient temperature in this case was 240.6K and the ambient pressure was 39.27 kPa. Two levels of RH_i, 110% and 100%, were investigated, and the simulation was performed up to 1000 m downstream. As shown in Figure 8, mixed results were obtained, where marked ice particle growth were observed for some initial soot particle number densities and sizes but not for others. This may be because that the formation of ice particle nuclei is very sensitive to the parametric space we are investigating here, particularly near the threshold for contrail formation.

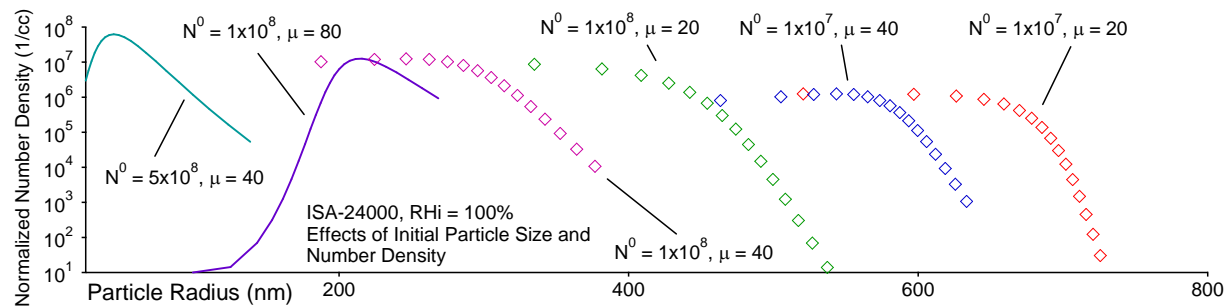


Figure 3. Effects of initial soot particle properties on ice particle size distributions at 1000 m downstream under ISA-24,000 conditions and ambient RH_i of 100%.

Recommended Future Work

We recommend comparing our one-dimensional modeling results with high fidelity Computation Fluid Dynamics (CFD) data as the next step. CFD calculations with detailed ice formation microphysics included will improve our understanding of formation mechanisms of early contrail and contrail-cirrus in a more comprehensive way. However, complete CFD calculations with complex microphysics included is usually very computational expensive. Results from our

one-dimensional modeling approach will provide useful insights for the CFD models to identify conditions of interest and important microphysics for detailed flow field simulations. Another recommended future work is to understand the conditions and thresholds for contrail formation from near-field aircraft emissions. In this case, an improved one-dimensional model may be developed to perform microphysical calculations near the threshold(s) of contrail formation parametrically.

References

- Davidson, M. J. and Wang, H. J. "Strongly Advected Jet in a Coflow," *J. Hydraulic Eng.*, 128, 742, 2002.
- Fuchs, N. A. *The Mechanics of Aerosols*. 1989.
- Garnier F., Brunet, S., Jacquin, L. "Modelling Exhaust Plume Mixing in the Near Field of an Aircraft," *Annales Geophysicae*, 15, 1468, 1997.
- Jacobson, M. Z. and Turco, R. P. "Simulating Condensational Growth, Evaporation, and Coagulation of Aerosols Using a Combined Moving and Stationary Size Grid," *Aerosol Sci. Technol.*, 22, 73, 1995.
- Kärcher, B. "On the Potential Importance of Sulfur-Induced Activation of Soot Particles in Nascent Jet Aircraft Exhaust Plumes," *J. Geophys. Res.*, 103, 17111, 1998.
- Lee, R. J., Rupley, F. M. and Miller, J. A. *CHEMKIN-III Documentation*, 1996.
- Penner, J. E., D. H. Lister, D. J. Griggs, D. J. Dokken, and M. McFarland (eds.), "Aviation and the Global Atmosphere", International Panel on Climate Change (IPCC) Special Report, Cambridge University Press, Cambridge, UK, 1999.
- Seinfeld, J. H. and Pandis, S. N. *Atmospheric Chemistry and Physics*, 1998.
- Schumann, U. Schlager, H., Arnold, F., Baumann, R., Haschberger, P. and Klemm, O. "Dilution of Aircraft Exhaust Plumes at Cruise Altitudes," *Atmos. Environ*, 32, 3097, 1998.
- Wuebbles, D., A. Douglass, B. Kärcher, W.-C. Wang, S. Baughcum, R. P. d'Entremont, A. Dessler, P. Ginoux, R. Herman, A. Heymsfield, I. Isaksen, D. Jacob, S. Lele, J. Logan, J. McConnell, R. Miake-Lye, P. Minnis, D. Mitchell, D. Murphy, L. Pan, J. Penner, M. Prather, J. Rodriguez, K. Rosenlof, K. Sassen, R. Sausen, K. Shine, A. Tabazadeh, I. Waitz, P. Yang, and F. Yu, "Workshop on the Impacts of Aviation on Climate Change: A Report of Findings and Recommendations", PARTNER-COE-2006-004, Aug. 2006.
- Wong, H.-W., Yelvington, P. E., Timko, M. T., Onasch, T. B., Miake-Lye, R. C., Zhang, J., and Waitz, I. A. "Microphysical Modeling of Aerosol Formation in Near-Field Aircraft Plumes at Ground Level," *J. Propul. Power*, submitted, 2007.
- Yu, F. "Quasi-Unary Homogeneous Nucleation of H₂SO₄-H₂O," *J. Chem. Phys.*, 122, 07451, 2005.
- Yu, F. "From Molecular Clusters to Nanoparticles: Second Generation Ion-Mediated Nucleation Model," *Atmos. Chem. Phys.* 6, 5193, 2006.
- Yu, F. "Improved Quasi-Unary Nucleation Model for Binary H₂SO₄-H₂O Homogeneous Nucleation," *J. Chem. Phys.*, 127, 054301, 2007.